Future Climate Change under SSP Emission Scenarios with GISS-E2.1

Larissa S. Nazarenko[1,2], Nick Tausnev[3,2], Gary L. Russell[2], David Rind[2], Ron L. Miller[2,4], Gavin A. Schmidt[2], Susanne E. Bauer[2], Maxwell Kelley[2], Reto Ruedy[3,2], Andrew S. Ackerman[2], Igor Aleinov[1,2], Michael Bauer[1,2], Rainer Bleck[5,6], Vittorio Canuto[2], Grégory Cesana[1,2], Ye Cheng[1,2], Thomas L. Clune[7], Ben I. Cook[2], Carlos A. Cruz[7,8], Anthony D. Del Genio[2], Gregory S. Elsaesser[4,2], Greg Faluvegi[1,2], Nancy Y. Kiang[2], Daehyun Kim[9], Andrew A. Lacis[2], Anthony Leboissetier[3,2], Allegra N. LeGrande[2], Ken K. Lo[3,2], John Marshall[10], Elaine E. Matthews[2], Sonali McDermid[11], Keren Mezuman[1,2], Lee T. Murray[12], Valdar Oinas[3,2], Clara Orbe[2], Carlos Pérez García-Pando[13,14], Jan P. Perlwitz[15,2], Michael J. Puma[1,2], Anastasia Romanou[2], Drew T. Shindell[16], Shan Sun[6], Kostas Tsigaridis[1,2], George Tselioudis[2], Ensheng Weng[1,2], Jingbo Wu[4,2], and Mao-Sung Yao[3,2]

[1]Center for Climate Systems Research, Earth Institute,Columbia University, New York, NY, USA

[2]NASA Goddard Institute for Space Studies, New York, NY, USA

[3] ciSpace LLC, New York, NY, USA

[4]Department of Applied Physics and Applied Mathematics, Columbia University, New York, NY, USA

[5]CIRES, University of Colorado Boulder, Boulder, CO, USA

[6]NOAA/ESRL/Global Systems Laboratory, Boulder, CO, USA

[7]Goddard Space Flight Center, Greenbelt, MD, USA, 8SSAI, Greenbelt, MD, USA

[9]Department of Atmospheric Sciences, University of Washington, Seattle, WA, USA

[10]Department of Earth, Atmospheric and Planetary Sciences, Massachusetts Institute of Technology, Cambridge MA, USA

This article has been accepted for publication and undergone full peer review but has not been through the copyediting, typesetting, pagination and proofreading process, which may lead to differences between this version and the Version of Record. Please cite this article as doi: 10.1029/2021MS002871.

[11]Department of Environmental Studies, New York University, New York, NY, USA

[12]Department of Earth and Environmental Sciences, University of Rochester, Rochester, NY, USA

[13]Barcelona Supercomputing Center, Barcelona, Spain

[14]ICREA, Catalan Institution for Research and Advanced Studies, Barcelona, Spain

[15]Climate, Aerosol, and Pollution Research, LLC, Bronx, NY, USA

[16]Nicholas School of the Environment, Duke University, Durham, NC, USA

Corresponding author:

Larissa Nazarenko

NASA Goddard Institute for Space Studies,

Center for Climate Systems Research, Columbia University,

2880 Broadway, New York, NY 10025

(larissa.s.nazarenko@nasa.gov)

Key Points:

- GISS E2.1 model with different configurations is used to carry out 134 SSP experiments
- GISS-E2.1 climate model shows a stronger warming by 2100 in comparable RCP scenarios in CMIP5 due to larger effective climate sensitivity and stronger transient climate response
- Both coupled models, E2.1-G and E2.1-H, project decreases in the Atlantic overturning stream function by 2100 with the largest decrease in the warmest scenario SSP5-8.5 in the E2.1-G model

Abstract

This paper presents the response to anthropogenic forcing in the GISS-E2.1 climate models for the 21st century Shared Socioeconomic Pathways (SSPs) emission scenarios within the Coupled Model Intercomparison Project phase 6 (CMIP6). The experiments were performed using an updated and improved version of the NASA Goddard Institute for Space Studies (GISS) coupled general circulation model that includes two different versions for atmospheric composition: a non-interactive version (NINT) with prescribed composition and a tuned aerosol indirect effect (AIE) and the One-Moment Aerosol model (OMA) version with fully interactive aerosols which includes a parameterized first indirect aerosol effect on clouds. The effective climate sensitivities are 3.0ºC and 2.9ºC for the NINT and OMA models, respectively. Each atmospheric version is coupled to two different ocean general circulation models: the GISS ocean model (E2.1-G) and HYCOM (E2.1-H). We describe the global mean responses for all future scenarios and spatial patterns of change for surface air temperature and precipitation for four of the marker scenarios: SSP1-2.6, SSP2-4.5, SSP4-6.0, and SSP5-8.5. By 2100, global mean warming ranges from 1.5ºC to 5.2ºC relative to 1850-1880 mean temperature. Two high-mitigation scenarios SSP1-1.9 and SSP1-2.6 limit the surface warming to below 2°C by the end of the **21st** century, except for the NINT E2.1-H model that simulates 2.2°C of surface warming. For the high emission scenario SSP5-8.5, the range is 4.6-5.2ºC at 2100. Due to about 15% larger effective climate sensitivity (ECS) and stronger transient climate response (TCR) in both NINT and OMA CMIP6 models compared to CMIP5 versions, there is a stronger warming by 2100 in the SSP emission scenarios than in the comparable RCP scenarios in CMIP5. Changes in sea ice area are highly correlated to global mean surface air temperature anomalies and show steep declines in both hemispheres, with the largest sea ice area decreases occurring during September in the Northern Hemisphere in both E2.1-G (-1.21×10^6 km^2/°C) and E2.1-H models (-0.94×10^6 km^2/°C). Both

coupled models project decreases in the Atlantic overturning stream function by 2100. The largest decrease of 56-65% in the 21st century overturning stream function is produced in the warmest scenario SSP5-8.5 in the E2.1-G model, comparable to the reduction in the corresponding CMIP5 GISS-E2 RCP8.5 simulation. Both low-end scenarios SSP1-1.9 and SSP1-2.6 also simulate substantial reductions of the overturning (9-37%) with slow recovery of about 10% by the end of the 21st century (relative to the maximum decrease at the middle of the 21st century).

Plain Language Summary

The projections of future climate change are uncertain because they are dependent on different possible scenarios of human-caused emissions and their interaction with natural forcings, internal climate variability, and inter-model differences. This paper presents the results of the climate model of the NASA Goddard Institute for Space Studies, GISS-E2.1, for the anthropogenically forced climate response for the twenty first century Shared Socioeconomic Pathways emission scenarios within the Coupled Model Intercomparison Project phase 6 (CMIP6). The sensitivity of the model response to different magnitudes of anthropogenic forcings in the twenty-first-century scenarios were performed using two different versions for the atmospheric composition and two different ocean general circulation models. Compared to CMIP5 GISS-E2 versions, the CMIP6 GISS-E2.1 climate model shows a stronger warming by 2100 in comparable scenarios due to larger ECS and TCR. Both climate models with two different ocean components project decreases in the Atlantic overturning stream function by 2100.

1. Introduction

Storyline-based scenarios based on plausible socio-economic pathways are required to study future projections of climate change. These scenarios are used to coordinate numerical experiments by modeling centers and contrast possible futures and the outcome of choices with respect to a range of socio-economic variables including technological change, energy and land use, inequality, and subsequent emissions of greenhouse gases and air pollutants. In the past, several sets of scenarios have performed such a role, including the scenarios from the Special Report on Emission Scenarios [*Nakicenovic et al.*, 2000], followed by the scenarios from Representative Concentration Pathways (RCPs) [*van Vuuren et al*, 2011], and more recently, the ScenarioMIP that combined the RCP/SSP forcing scenarios to conduct integrated assessments of responses to various strategies with respect to mitigations and adaptations to climate change [*O'Neill et al.,* 2016]. Nine ScenarioMIP scenarios are continuations of the CMIP6 historical (1850-2014) experiments.

Since confident prediction of future socio-economic change is impossible, examining a broad range of scenarios has been a key component of climate change research for four decades. The future developments of anthropogenic drivers of climate change are unknown. Therefore, a wide range of future scenarios were produced with integrated assumptions based on economic, social, and technological developments as well as environmental conditions. They are used as input for climate model runs to estimate the responses to a range of the alternative conditions, as well as for exploring potential feedbacks and sensitivities. To serve a wide range of scientific research studies, nine alternative 21st century scenarios were developed [*O'Neill et al.,* 2016].

Here we use the GISS-E2.1 climate model [*Kelley et al*., 2020] to explore the sensitivity of the model response to different magnitudes of anthropogenic forcings in the wide range of the twenty-first-century ScenarioMIP scenarios, as well as the response of the climate system

simulated with different model representations. The main focus of this paper is to provide a summary overview of the GISS climate simulations of the 21st century ScenarioMIP scenarios, to present estimates of global climate change and some impacts on regional temperature and precipitation with different versions of the GISS climate model, noting the differences with respect to the CMIP5 GISS simulations [*Nazarenko et al.*, 2015]. In Section 2, we present a brief description of different versions of the GISS climate model. *Kelley et al.* [2020] describes the GISS climate model in greater detail including improvements of model physics as well as the evaluation of the seasonal climatology of the atmospheric and coupled models during the satellite period (1979-2014), while *Miller et al.* [2021] describes the drivers and responses over the historical period (1850-2014). Section 3 describes the SSP emission scenarios and forcings applied for 21st century simulations. Global changes for the SSP experiments are discussed in Section 4, while regional changes are presented in Section 5. Section 6 describes the projections of the annular modes in the Northern and Southern Hemispheres. Conclusions are presented in Section 7.

2. Model Description

2.1. Atmospheric Models

We use a new version of the NASA Goddard Institute for Space Studies (GISS) climate model, GISS-E2.1 with unchanged horizontal and vertical resolution since CMIP5: 2º latitude by 2.5º longitude with 40 vertical layers, with the model top near the stratopause at 0.1 hPa. A more complete description of GISS-E2.1 including numerous improvements to the physics since CMIP5 is provided in *Kelley et al.* [2020] and *Miller et al.* [2021]. Many details of composition modelling and performance over the historical period (1850-2014) are presented in *Bauer et al.* [2020].

We use two different treatments of the atmospheric composition. The simplest is a version with Non-INTeractive (NINT) composition. Three-dimensional monthly mean distributions of aerosols and ozone are prescribed from atmosphere-only simulations of the fully interactive aerosol and chemistry model. The aerosol indirect effect on clouds is included as a simple parameterization for increasing the low cloud cover in response to increasing aerosols [*Hansen et al.,* 2005]. This parameterization is based on an assumed relation between aerosol number concentrations and cloud fraction and tuned to produce a roughly -1.0 W/m^2 of forcing in 2000 relative to 1850 (see *Miller et al.* [2021] for a discussion).

The second version (OMA – One-Moment Aerosol model) has fully interactive aerosols [*Bauer et al.,* 2020] and chemistry in both the troposphere and stratosphere [*Shindell et al.,* 2013]. All chemical species are simulated prognostically consistent with atmospheric physics in the model and the emissions of short-lived precursors. The OMA model includes a parameterization of the first indirect aerosol effect on clouds relating aerosol concentration to cloud optical thickness [*Twomey,* 1977; *Menon et al.,* 2010]. In the CMIP6 archive, the NINT and OMA runs are denoted as physics-version=1 and 3, respectively.

2.2. Ocean Models

We couple two different ocean general circulation models to each of the two atmospheric versions. The E2.1-G uses the GISS Ocean version 1 (GO1), a descendant of the "Russell ocean model" originally described by *Russell et al.* [1995]. This ocean model is a mass conserving with horizontal resolution of 1.25° longitude by 1° latitude and has 40 vertical levels with finer resolution in the top 100 m, which is 8 more layers than in the CMIP5 version. The model uses the C-grid for the momentum equations, includes the KPP parameterization for vertical mixing [*Large*

et al., 1994] and a modified Gent-McWilliams parameterization for the mixing effect associated with mesoscale eddies [*Gent and McWilliams*, 1990; *Kelley et al.*, 2020]. The other ocean model used for climate simulations is HYCOM [*Bleck*, 2006; *Sun and Bleck*, 2006], the HYbrid coordinate version of the Miami Isopycnal Coordinate Ocean Model. The E2.1-H model increased the number of vertical layers to 32 from 26 in CMIP5 E2-H. While it maintains an isopycnal coordinate representation in the oceanic interior, it allows coordinate layers to become constant in depth poleward of the location where their ‘‘target’’ isopycnals outcrop. The horizontal resolution is nominally 1° both in latitude and longitude. The improvements to the physics since CMIP5 for both ocean models were documented in the paper by *Kelley et al.* [2020].

Both ocean models include the same model of sea ice dynamics in the Arctic and Antarctic [*Zhang and Rothrock*, 2000]. The sea ice thermodynamics model has modifications such as a brine pocket parameterization and independent advection of snow mass along with removal of leads for multi-year Arctic ice [*Schmidt et al.*, 2004; *Kelley et al.*, 2020].

3. Shared Socioeconomic Pathway Experiments

Projections of future climate change represent assessments of possible changes that depend on many anthropogenically forced factors, such as greenhouse gases, chemically reactive gases, aerosols, and land use. In the SSP experiments [*Meinshausen et al.*, 2020], the total radiative forcings (Fig. 1a) are largely determined by well-mixed greenhouse gases (Fig. 1b) moderated by radiative forcings from tropospheric aerosols (Fig. 1c). The GHG concentrations are provided by SSP projections. The dominant component of the GHG concentrations is carbon dioxide for most SSP emission scenarios (Fig. 2a, Table 1).

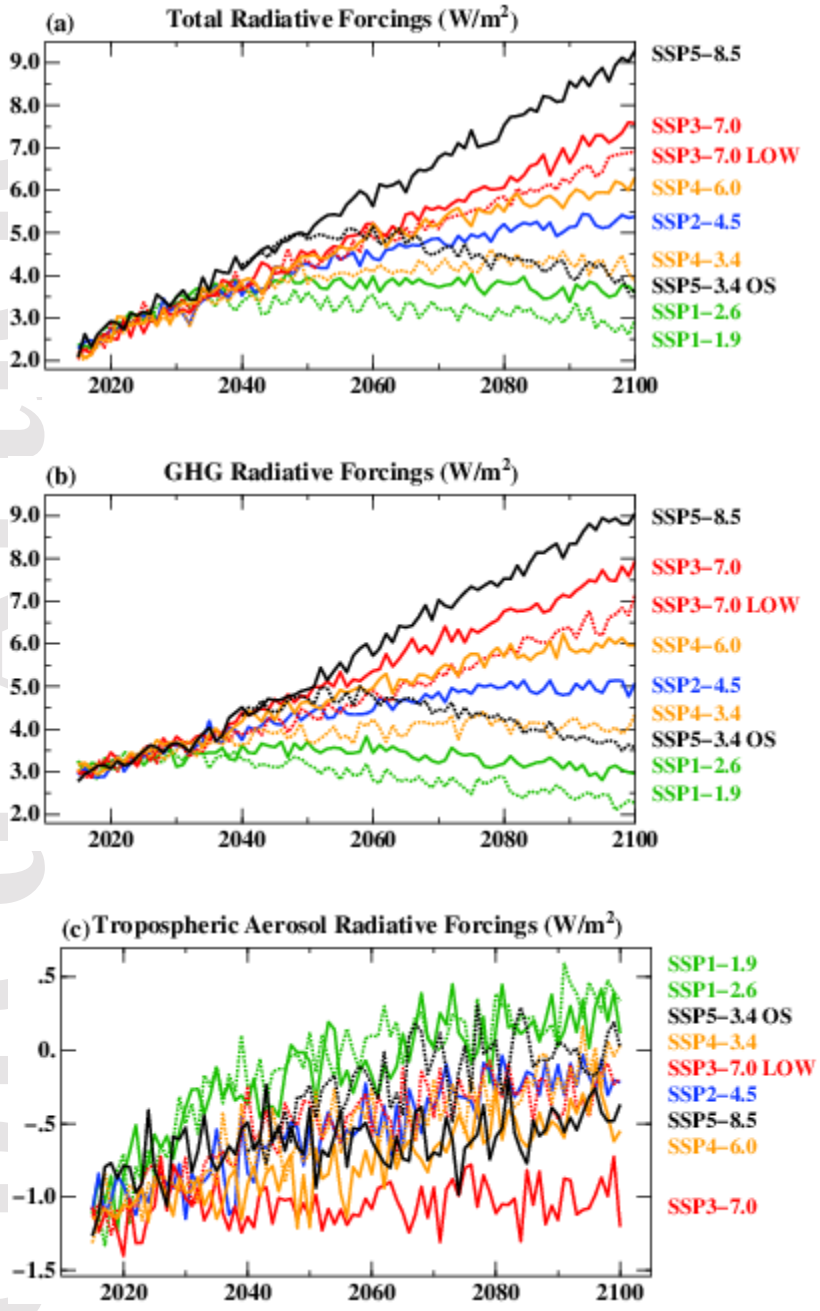

Figure 1. Effective radiative forcings diagnosed for global future climate simulations in the E2.1-G NINT models.

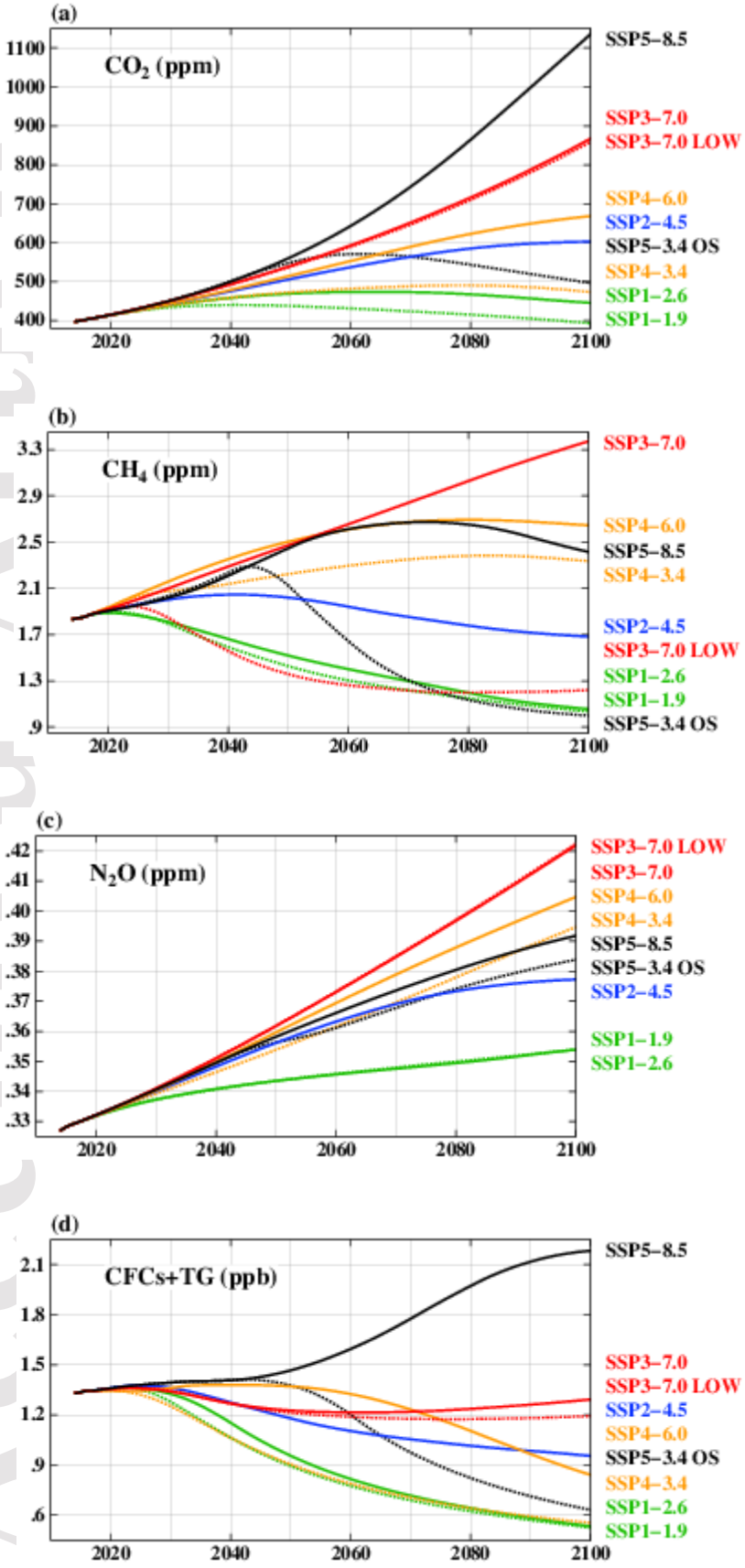

Figure 2. Greenhouse gas mixing ratios in the E2.1-G NINT SSP **emission** scenarios.

The nominal radiative forcings for SSP runs range from 1.9 W/m^2 to 8.5 W/m^2. Based on climate change or climate policy, eight ScenarioMIP scenarios were divided into 5 groups. SSP1 includes two future experiments with 1.9 W/m^2 and 2.6 W/m^2 for the total radiative forcings. SSP1 is the Green Road experiment with the emphasis on reduction of anthropogenic emissions, on transition to renewable energy supplies, on educational and health investments [*van Vuuren et al.*, 2017]. SSP2 with 4.5 W/m^2 of total radiative forcing is a Middle of the Road experiment that continues the patterns of the historical simulation in terms of anthropogenic emissions and developments in environmental systems [*Frisco et al.*, 2017]. SSP3 with high radiative forcing of 7.0 W/m^2 reflects the path with high air pollutant emissions, expansion of cropland, fast growing population with little investments in education and health [*Fujimori et al.*, 2017]. It includes two high scenarios SSP3-7.0 and SSP3-7.0LOW that have two different evolutions of the near-term climate forcers. The effective radiative forcings for the greenhouse gases differ by about 1 W/m^2 for these two scenarios (Fig. 1b). SSP4 is the experiment with large inequalities between and within regions where high-income communities prosper and low-income regions experience limited economic growth. Due to different levels in regional air pollution, the radiative forcing reaches 6.0 W/m^2 globally. SSP4-6.0 is similar to the CMIP5 RCP6.0 by its projection and effects. SSP4 also includes the scenario with rather low radiative forcing of 3.4 W/m^2 that fills the gap between the low and the high ends of the range of future forcing pathways [*Calvin et al.*, 2017]. The upper end of the future scenarios is SSP5 with the highest radiative forcing of 8.5 W/m^2 due to very high levels of fossil fuel use that leads to a tripling of the greenhouse emissions over the course of the 21st century [*Kriegler et al.*, 2017]. SSP5 also includes the SSP5-3.4OS scenario that

continues after the year 2040 of the SSP5-8.5 with the substantial decline in forcing during the 21st century. All SSP experiments were carried out from 2015 to 2100.

The projected CO_2 concentrations range from 393 to 1135 ppm in 2100, with the low scenario SSP1-1.9 decreasing to 350 ppm by 2150. In the high scenario SSP5-8.5, the CO_2 concentration is projected to increase up to 2200 ppm by 2250.

The projected methane (CH_4) concentrations provided as part of the SSPs are the largest for SSP3-7.0 that almost doubles at 2100 relative to 2015. In the high scenario SSP3-7.0LOW, the CH_4 concentrations increase slightly and then steadily decrease by about a third by 2100. The largest decrease in the CH_4 concentration is projected in SSP5-3.4OS where it is reduced by more than a half by 2100. In this scenario, the CH_4 concentration is lower at 2100 than in the low scenarios SSP1-1.9 and SSP1-2.6 (Fig. 2b).

In the OMA model with fully interactive composition, CH_4 concentrations are calculated based on prescribed anthropogenic emissions and prognostic atmospheric chemistry and natural emissions. The OMA model shows higher methane concentrations than the ones from the prescribed SSP concentrations (Fig. 3) because of positive feedbacks via atmospheric chemistry (i.e. an increased methane lifetime) and increased wetland emissions. A similar difference of methane concentration in the non-interactive and fully prognostic models was also seen in the CMIP5 models [*Shindell et al.*, 2013; *Nazarenko et al.*, 2015].

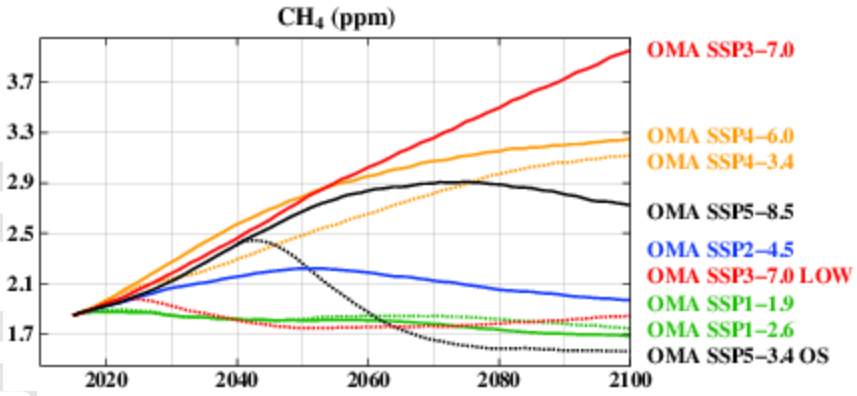

Figure 3. CH_4 mixing ratios in the E2.1-G OMA SSP **emission** scenarios.

The nitrous oxide (N_2O) concentrations are projected to increase for all scenarios (Fig. 2c). For the lowest emission scenarios SSP1-1.9 and SSP1-2.6, the N_2O concentrations increase by about 30 ppb by 2100. The largest increases in N_2O concentrations are expected in SSP3-7.0 and SSP3-7.0LOW, and they are projected to increase by almost 100 ppb by 2100 (Fig. 2c).

The projected concentrations of ozone-depleting substances, such as CFCs and other trace gases, decrease for six out of nine modeled scenarios (Fig. 2d). In the high scenario SSP5-8.5, the CFC and trace gas concentrations are assumed to have strong increases for most of the 21st century. In two other high scenarios SSP3-7.0 and SSP3-7.0LOW, there are no substantial variations in the projected concentrations of CFCs and other trace gases.

The effective radiative forcings (ERFs) in the GISS models for the greenhouse gases presented in Fig. 1b shows that the largest forcing of the SSP5-8.5 scenario is 9 W/m^2 at the year 2100. In the multimodel analysis by *Smith et al.* [2018], CO_2 is suggested to have a slightly (~5%) higher ERF than its instantaneous radiative forcing after stratospheric temperature adjustments alone. Since the contribution of CO_2 is the largest, the ERFs of the greenhouse gases are consistently greater than the nominal forcings for all scenarios. Decrease of methane concentration in the scenario SSP3-7.0LOW (Fig. 2b) is reflected in smaller greenhouse gas forcings at the year

2100 compared to the GHG forcings in the scenario SSP3-7.0 (Fig. 1b). A steady reduction of both CO_2 and methane after 2050s in the scenario SSP5-3.4OS leads to projected decline in the greenhouse gas forcings from about 5 W/m^2 in 2050s to about 3.6 W/m^2 at the year 2100. In both low-end scenarios SSP1-1.9 and SSP1-2.6, the greenhouse gas forcings at the year 2100 are smaller than at the start of these scenarios (Fig. 1b).

The ERFs for tropospheric aerosols presented in Fig. 1c are calculated with the NINT model. First, the CMIP6 emissions for nine ScenarioMIP scenarios [*Riahi et al.,* 2017; *Gidden et al.,* 2019] were applied to the SSP experiments in the OMA version of the coupled model with interactive chemistry and aerosols. These tropospheric aerosol distributions were extracted and prescribed in the NINT model to calculate the ERFs for all ScenarioMIP scenarios. These non-interactive model calculations are useful for estimating ERF considering internal model variability. Fig. 1c shows that the year-to-year variations of the ERFs for the tropospheric aerosols is about 0.3 W/m^2 for all scenarios, and it is comparable to year-to-year standard deviations for the last decade of the historical simulations. For the low-end scenarios SSP1-1.9 and SSP1-2.6, the ERFs are smaller or comparable to the year-to-year variations. To make a more precise estimate of the ERFs for the tropospheric aerosols, averages over the last decade, 2091-2100, were used and compared to the last decade of the historical time interval, 2005-2014. The ERFs of tropospheric aerosols are -1.2 W/m^2 and -0.1 W/m^2 for 2005-2014 and for 1850-1859, respectively.

Compared to 2005-2014, the negative ERFs for tropospheric aerosols is weaker in all scenarios (Fig. 1c), except in SSP3-7.0 which has the highest aerosol burden. In SSP3-7.0, the mid-2090s ERFs of about -1.0 W/m^2 is a little weaker than the estimate for the historical 2005-2014 interval of -1.2 W/m^2. Reduction of aerosol emissions in the scenarios SSP1-1.9 and SSP1-2.6 results in substantial change from the negative effective aerosol forcing in the historical

simulations to the positive forcing of about 0.3 W/m^2 for the mid-2090s. For the other six scenarios, the ERFs of anthropogenic aerosols ranges from -0.1 W/m^2 for SSP4-3.4 and SSP5-3.4OS to about -0.4 W/m^2 for SSP4-6.0 and SSP5-8.5.

Modelling-based estimates of the ERFs for tropospheric aerosols [*Partanen et al.,* 2018; *Fiedler et al.,* 2019; *Lund et al.,* 2019] show a broad range in forcings, from -0.02 W/m^2 to -0.92 W/m^2 in 2100 (relative to 1850). While not directly comparable due to differences in the simulated aerosol distributions, optical properties and cloud fields, all studies conclude that weak air pollution control over the 21st century would result in strong negative aerosol forcing. Air quality controls lead to rapid weakening of the negative aerosol forcings, which will unmask more of the greenhouse gas induced warming.

Figure 1a shows that the total ERFs for all ScenarioMIP scenarios are larger in the GISS-E2.1 model than the nominal forcings [*Riahi et al.,* 2017]. The results from international comparison projects indicate that the ScenarioMIP scenario forcings may be attainable at equilibrium while some models find that some forcing targets are unattainable, in particular the low forcing targets of 1.9 and 2.6 W/m^2 [*Clarke et al.,* 2009; *Kriegler et al.,* 2014]. Note that because climate models have different implementations for calculations of radiative forcing given their greenhouse gases and aerosols, the results shown here are indicative of the GISS models, and may differ from other models [*Meinshausen et al.,* 2020].

The land-use change components cover a wide-varying range of possible futures in the ScenarioMIP scenarios [*Riahi et al.,* 2017]. SSP land use changes are based on assumed regulations, demands, productivity, environmental impacts, trade, and the degree of globalization of future agricultural and forestry markets [*Popp et al.,* 2017]. For GISS-E2.1, we classified the *Riahi et al.* [2017] land cover by merging the crop and pasture cover types into the model's single

C3 crop type; the change in this cover type was used to rescale the cover of natural vegetation, as described in *Ito et al.* [2020].

In all nine ScenarioMIP scenarios, volcanic aerosol forcing ramped up from the value at the end of the historical simulation period (2015) over 10 years to the same constant value (background stratospheric aerosols) prescribed for the pre-industrial simulations, and was then kept fixed [*O'Neill et al.,* 2016]. For the solar forcing, we repeat the last 11-year solar cycle of the historical simulation consistent with the CMIP5 approach [*Meinshausen et al.,* 2011].

We carried out 134 SSP experiments with different configurations of the GISS E2.1 model. The number of ensemble members for each SSP experiment and model configuration is indicated in Table 1. For the line plots of the annual mean quantities for each ScenarioMIP scenario, the data were averaged for all versions of atmospheric and ocean models. The range of the SSP results is given by different shading for each SSP case with the NINT and OMA E2.1-G and E2.1-H climate models. The maps present the means of the NINT models with five ensemble members for both E2.1-G and E2.1-H for SSP1-2.6 and SSP5-8.5 scenarios, with ten ensemble members for E2.1-G and five ensemble members for E2.1-H for SSP2-4.5 scenario, with five ensemble members for E2.1-G and one member for E2.1-H for SSP4-6.0 scenario. To compare the regional difference between OMA and NINT, and E2.1-H and E2.1-G, the averages were made over all versions and ensemble members of E2.1-G and E2.1-H simulations for SSP2-4.5 scenario.

4. Global Changes

4.1. Global Temperature and the Planetary Energy Imbalance

Figure 4 shows the simulated global mean surface air temperature (drift-corrected) anomalies relative to the 1850-1880 base period. The low-frequency drift of the model was

subtracted from each ensemble member for all SSP emission scenarios as described in *Miller et al.* [2021]. During the historical simulation, the global mean surface air temperature essentially follows the estimated global mean forcing through time, showing cooling following the short-term forcing by volcanic aerosols and strong warming for a few decades at the end of the 20th century due to the dominant positive forcing of the increasing greenhouse gases. Simulated global warming is about 1.0°C between 1850 and 2014 and agrees well with the observed temperature increase, which is estimated also as about 1.0°C [*Lenssen et al.*, 2019] (see *Miller et al.*, [2021] for more discussion of the 20th century changes and comparison to observations).

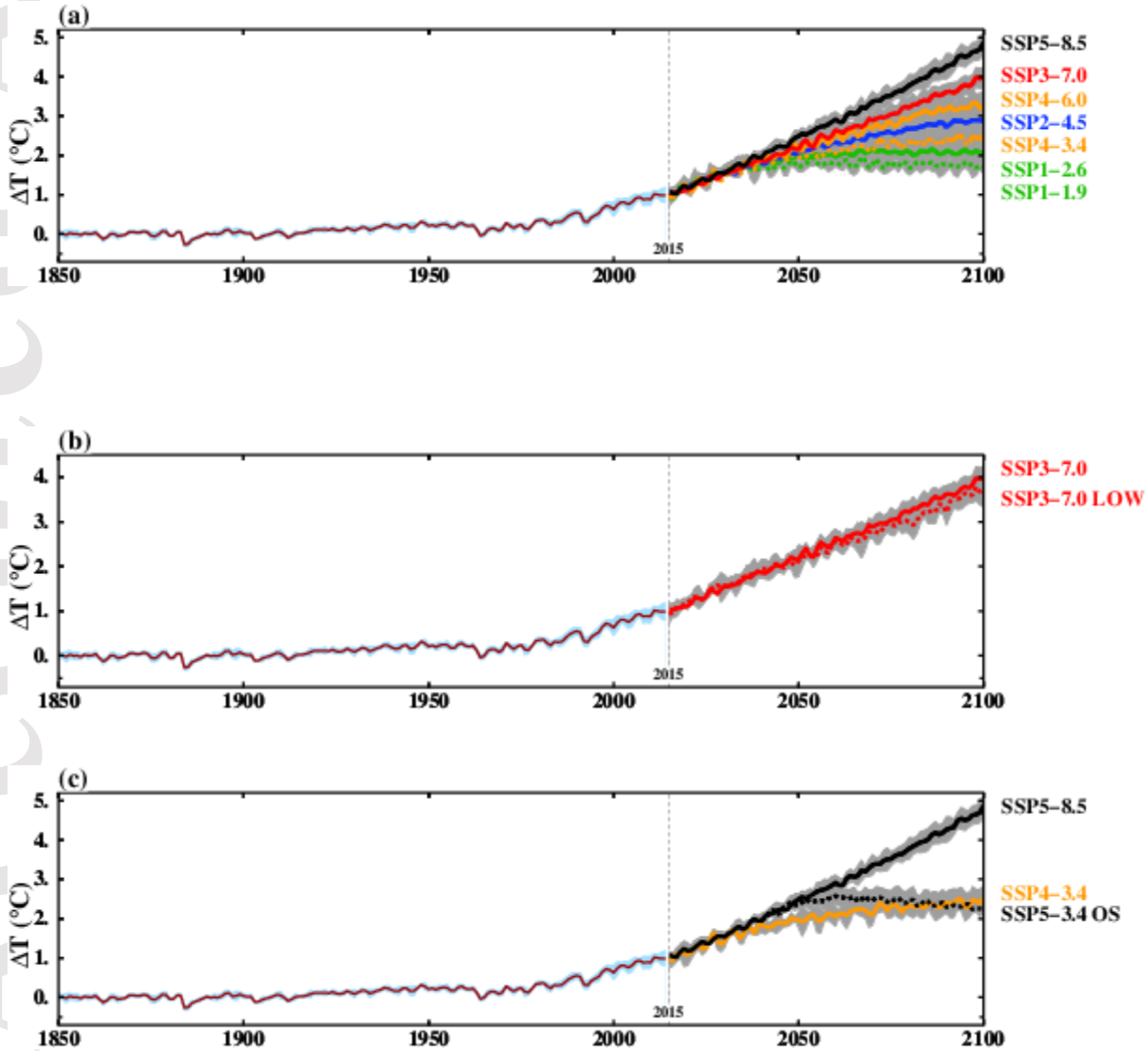

Figure 4. Global annual mean surface air temperature anomalies relative to the 1850-1880 base period for all SSP emission scenarios. The data were averaged for all versions of atmospheric and ocean models. Different shadings indicate ranges of the SSP experiments with the NINT and OMA E2.1-G and E2.1-H climate models.

Relative to the last decade (2005-2014) in the historical simulations, the simulated global warming in the SSP experiments ranges between 0.5°C and 1.6°C at 2050 (Table 1). For all SSP experiments except for SSP1-1.9 and SSP1-2.6, the additional warming of global mean surface air temperature increases and exceeds 1°C by 2100. In the SSP1-1.9 and SSP1-2.6 scenarios, both NINT and OMA versions of E2.1-G show decreases in temperature by 2100 reflecting the design of these scenarios with anticipated warming below 1.5 and 2.0°C in 2100, respectively [*O'Neill et al.*, 2016]. The E2.1-H model has a higher TCR than E2.1-G (Table 6 from *Kelley et al*, 2020). Both NINT and OMA configurations of the E2.1-H model simulated stronger warming over the last decades of the historical period compared to the E2.1-G configurations (Table 6 from *Miller et al.* [2021]) that continued with stronger warming for all scenarios in the E2.1-H models.

Table 1. Surface air temperature change (°C) relative to (2005-2014)-mean temperature for different years in the future. The number of ensemble members for each SSP experiment and model configuration is indicated in brackets.

SSP Experiment	2050	2100	2200	2300	2400	2500	2100[&]
SSP1-1.9 NINT-G (5)	0.9±0.16	0.7±0.13					1.5±0.13
NINT-H (1)	0.8	0.9					1.9
OMA-G (1)	0.9	0.7					1.5
OMA-H (1)	0.5	0.8					1.9

SSP1-2.6 NINT-G (5)	1.1±0.09	1.1±0.06	1.1±0.16	1.0±0.12	1.0±0.11	1.0±0.17	1.9±0.06
NINT-H (5)	1.2±0.09	1.2±0.04	1.2±0.14	1.1±0.06	1.3±0.09	1.3±0.14	2.3±0.04
OMA-G (5)	1.1±0.12	1.0±0.08	1.1±0.15	0.9±0.09	0.9±0.09	1.0±0.23	1.8±0.08
OMA-H (5)	1.1±0.17	1.2±0.26	1.2±0.09	1.2±0.19	1.1±0.17		2.1±0.16
SSP4-3.4 NINT-G (5)	1.0±0.19	1.4±0.08					2.2±0.08
NINT-H (1)	1.1	1.9					2.9
OMA-G (1)	0.9	1.5					2.2
OMA-H (1)	1.1	1.6					2.8
SSP5-3.4OS NINT-G (5)	1.5±0.13	1.2±0.2	0.8±0.21	0.6±0.11			2.0±0.2
NINT-H (5)	1.5±0.12	1.6±0.18	1.0±0.09	1.1±0.16			2.5±0.18
OMA-G (5)	1.5±0.23	1.1±0.14	0.9±0.12	0.8±0.17			1.9±0.18
OMA-H (1)	1.2	1.5	1.0	0.6			2.6
SSP2-4.5 NINT-G (10)	1.2±0.08	1.8±0.12	2.1±0.15	2.3±0.28	2.3±0.41	2.1±0.3	2.7±0.31
NINT-H (5)	1.2±0.19	2.2±0.12	2.7±0.12	2.6±0.09	2.9±0.03	2.8±0.13	3.2±0.12
OMA-G (5)	1.1±0.13	1.8±0.27					2.6±0.41
OMA-H (5)	1.0±0.2	2.0±0.09					3.3±0.11
SSP4-6.0 NINT-G (5)	1.3±0.13	2.2±0.18					3.0±0.15
NINT-H (1)	1.0	2.7					3.7
OMA-G (1)	1.2	1.9					2.7
OMA-H (1)	1.2	2.3					3.4
SSP3-7.0 NINT-G (10)	1.3±0.13	2.9±0.14					3.7±0.14
NINT-H (5)	1.4±0.2	3.2±0.14					4.3±0.14
OMA-G (5)	1.1±0.21	3.0±0.21					3.8±0.21
OMA-H (1)	1.1	3.2					4.4
SSP3-7.0LOW NINT-G (5)	1.3±0.12	2.6±0.22					3.4±0.22

NINT-H (1)	1.5	3.1					4.1
OMA-G (1)	0.8	2.5					3.3
OMA-H (1)	1.2	3.0					4.1
SSP5-8.5 NINT-G (5)	1.6±0.15	3.8±0.06	6.5±0.15	7.2±0.06			4.6±0.06
NINT-H (5)	1.6±0.24	4.1±0.24	7.2±0.09	7.9±0.08			5.2±0.24
OMA-G (5)	1.5±0.12	3.8±0.09	6.6±0.08	7.4±0.09	7.6±0.07	7.6±0.12	4.6±0.09
OMA-H (5)	1.5±0.1	4.1±0.37					5.2±0.37

2100[&] column is surface air temperature change (°C) relative to (1850-1880)-mean temperature.

The GISS CMIP6 models show a slightly larger ECS (2.7-3.1°C) and TCR (1.8-2.0°C) in both NINT and OMA configurations compared to CMIP5 versions (2.1-2.5°C and 1.4-1.8°C) (Table 6 from *Kelley et al,* 2020). From the feedback analysis by *Zelinka et al.* [2020], both GISS E2.1-G and E2.1-H models simulate more positive shortwave feedback for the extratropical low clouds compared to the CMIP5 predecessors that has a direct contribution to the stronger warming. Comparing the E2.1-G and E2.1-H models, it is noted that the higher ECS in the GISS E2.1-H (3.1°C) configuration than in the E2.1-G (2.7°C) is due to bigger albedo effect [*Zelinka et al.*, 2020]. In addition to this, the contributions from both non-cloud and cloud feedbacks to ECS in the E2.1-H model are more positive compared to the E2.1-G model (Table S1 and Figure S7 from *Zelinka et al.* [2020]).

There is a stronger warming by 2100 in scenarios SSP2-4.5, SSP4-6.0, and SSP5-8.5 than in the comparable CMIP5 RCP scenarios. For the intermediate SSP2-4.5 and SSP4-6.0 scenarios, simulated global warming ranges between 2.0 and 2.9°C in 2100 relative to the 1996-2005 mean temperature while the warming was between 1.1 and 2.5°C in the CMIP5 RCP4.5 and RCP6.0

scenarios (Table 1 from *Nazarenko et al.*, 2015). In the high-end scenario SSP5-8.5, the 2100 warming is between 4.0 and 4.3°C versus 2.7-3.7°C in the CMIP5 RCP8.5 scenario.

Two high end scenarios SSP3-7.0 and SSP3-7.0LOW differ by smaller loads of the near-term climate forcers in the SSP3-7.0LOW (Fig. 2). In particular, the evolution of methane is opposite for these two scenarios (Fig. 2b) with a substantial decrease of methane by 2100 in SSP3-7.0LOW while it is almost doubled in SSP3-7.0 scenario. The total ERF is smaller by only 0.5 W/m^2 for SSP3-7.0LOW (Fig. 1a) due to reduction of negative effective forcings from the tropospheric aerosols (Fig. 1c). The temperature warming at 2100 ranges between 3.1 and 3.4°C in SSP3-7.0 versus 2.7 and 3.3°C in SSP3-7.0LOW (Table 1, Fig. 4b).

Figure 4c shows the temperature for three scenarios. The overshoot scenario SSP5-3.4OS branches from the year 2040 of the SSP5-8.5 scenario including the emission reduction rates after 2040 and reaching net negative emissions by the end of the century (Fig. 2). The ERFs for the greenhouse gases strongly decline by 2100 after reaching a peak around 2050 (Fig. 1b). Due to a reduction of tropospheric aerosol emissions (Fig. 1c), the total effective forcings for SSP5-3.4OS scenario approach those of SSP1-2.6 by 2100, which was the intention plan for this scenario (Fig. 1a) [*O'Neill et al.,* 2016]. The SSP5-3.4OS forcings are smaller than for a similar forcing scenario SSP4-3.4 leading to weaker warming between 1.1 and 1.6°C in SSP5-3.4OS versus 1.4 and 1.9°C in SSP4-3.4 by the year 2100 (Fig. 4c).

The year 2100 surface air temperature change relative to preindustrial (1850-1880) mean temperature are shown in the last column of Table 1. Only two low-end scenarios SSP1-1.9 and SSP1-2.6 project surface warming below 2°C by the end of the 21st century. Both NINT and OMA versions of E2.1-H model produce temperature increases of 2.3°C by 2100 for SSP1-2.6 although this model shows a gradual decrease of temperature during the extensions over the 21st and 22nd

centuries as do both NINT and OMA versions of E2.1-G model. Both NINT and OMA versions of E2.1-G limit warming to 1.5°C by 2100 in SSP1-1.9. The E2.1-H versions exceed 1.5ºC but stay below 2°C warming. **Six** out of eight versions meet the goal of staying below 2°C warming by 2100 in two low-end scenarios SSP1-1.9 and SSP1-2.6 (Table 1).

The climate system response to GHG and non-GHG forcings combined with radiative feedbacks is shown in Figure 5 as a planetary energy imbalance at the top of the atmosphere. The energy imbalance increased more than three times in the high-end scenario SSP5-8.5 over the 21st century while it declined to smaller than historical-end values in both low-end scenarios SSP1-1.9 and SSP1-2.6 (Fig. 5a). The decline of net radiation of the planet in both low-end scenarios implies the eventual achievement of a future equilibrium state. In the intermediate range SSP4-3.4 and SSP2-4.5 scenarios, there is a gradual decrease of energy imbalance reflecting the stabilization of both GHG and tropospheric aerosol forcings over the last 30-40 years of the 21st century (Fig. 1b, 1c). In three high end scenarios SSP4-6.0, SSP3-7.0 and SSP5-8.5, the continuous increase of energy imbalance is a result of steep increase in GHG forcing over the 21st century.

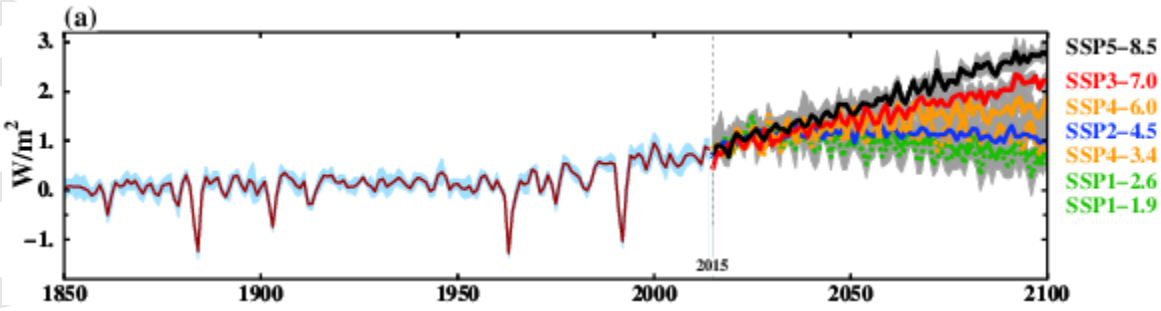

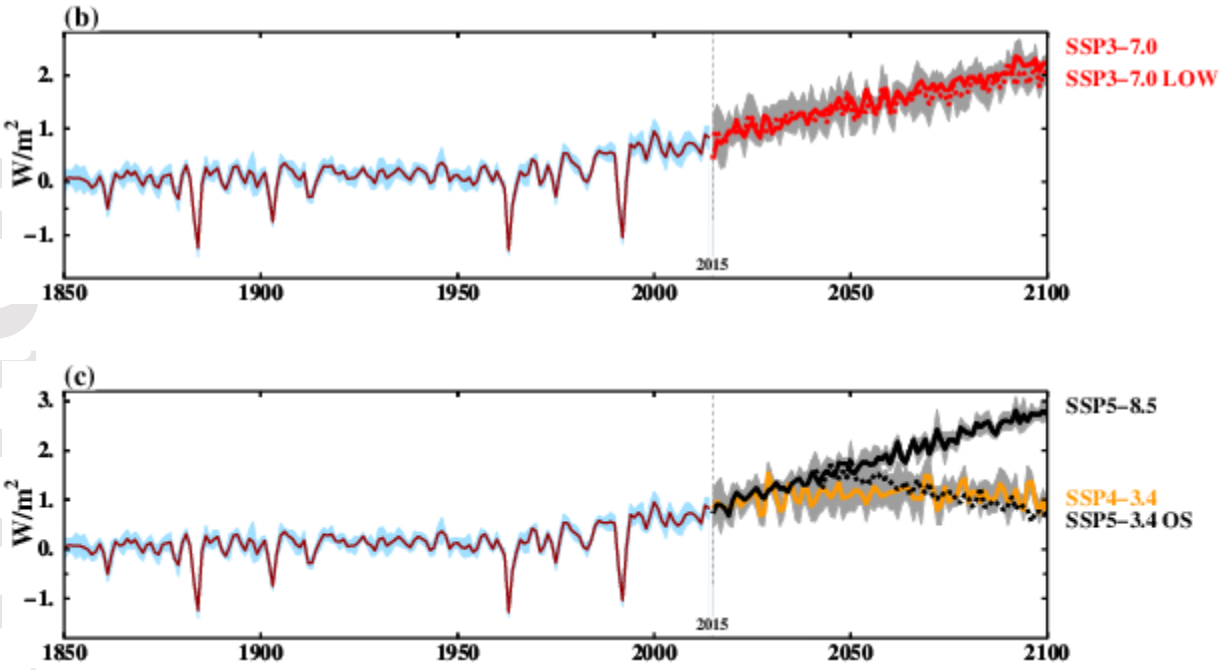

Figure 5. Net radiation at the top of the atmosphere (W/m^2).

Fig. 5b compares the energy imbalance of two high end scenarios SSP3-7.0 and SSP3-7.0LOW. There is a smaller impact of lower loads of GHGs in SSP3-7.0LOW (Fig. 1b). Since the negative forcings from the tropospheric aerosols are weaker in the SSP3-7.0LOW (Fig. 1c) compared to SSP3-7.0, the difference in total radiative forcings is smaller than the GHG forcings in these two scenarios (Fig. 1a). This led to a smaller energy imbalance in the SSP3-7.0LOW scenario (Fig. 5b).

Strong reduction of all anthropogenic forcings after 2040 in the overshoot scenario SSP5-3.4OS brings the energy imbalance to the level similar to the SSP4-3.4 scenario (Fig. 5c). The high-end scenario SSP5-8.5, the year 2040 of which was used for branching SSP5-3.4OS, differs noticeably despite a stronger negative tropospheric aerosol forcings (Fig. 1c). This suggests that aggressive reduction of emissions to zero by about 2070 and to net negative levels thereafter (Fig.

2) would lead to a rapid decrease of energy imbalance in SSP5-3.4OS over the last couple decades of the 21st century (Fig. 5c).

4.2 Sea Ice Changes

Over the historical time period, simulated sea ice area is greater in both hemispheres in the GISS-E2.1 model compared to the GISS CMIP5 versions [*Miller et al.,* 2021]. Nevertheless, over the satellite period, 1979-2012, simulated decline in hemispheric sea ice area (Fig. 17 from *Miller et al.*, 2021) is comparable to observed decrease [*Brennan et al.*, 2020]. In particular for the Northern Hemisphere (NH) sea ice cover, *Notz et al.* [2020] pointed out that the CMIP6 multimodel ensemble mean is very close to the observational estimate and well within the plausible range. GISS E2.1 is one of a few CMIP6 models that is able to simulate a plausible amount of sea-ice loss and simultaneously a plausible change in global mean temperature over time (or cumulative anthropogenic CO_2 emissions) [*Notz et al.*, 2020]. In addition to this, the amplitude of the seasonal cycle of sea ice extent has improved in both hemispheres in E2.1-G model [*Kelley et al,* 2020]. Sea ice distribution is similar in E2.1-H model although warmer conditions produce smaller sea ice cover in the end of the historical period compared to E2.1-G model [*Miller et al.*, 2021].

In response to stronger warming (Table 1), the NINT model simulates more sea ice decrease than the OMA configuration using both ocean variants and in all SSP experiments. For SSP5-8.5, the E2.1-H model shows the largest sea ice cover reductions which are 65% and 74% for the NH and Southern Hemisphere (SH) annual mean sea ice cover change based on the linear trend over the period 2015-2100, averaged for both NINT and OMA configurations (Table 2).

Table 2. Annual mean sea ice cover decrease **(**minus sign**)** based on linear trend over the period 2015-2100. The plus sign is the sea ice cover increase.

	E2.1-H		**E2.1-G**	
	NH	**SH**	**NH**	**SH**
SSP1-1.9	-9±1%	-9±7%	-12±1%	+6±4%
SSP1-2.6	-15±2%	-11±7%	-15±2%	+3±6%
SSP4-3.4	-20±4%	-23±6%	-13±2%	-2±4%
SSP2-4.5	-25±2%	-35±12%	-22±3%	-11±6%
SSP4-6.0	-28±1%	-35±3%	-24±1%	-14±6%
SSP3-7.0	-34±2%	-48±6%	-31±1%	-25±7%
SSP3-7.0LOW	-34±1%	-40±10%	-30±3%	-16±8%
SSP5-8.5	-65±27%	-74±23%	-39±3%	-40±8%
SSP5-3.4OS	+1±2%	-16±9%	+4±4%	+2±2%

The E2.1-G model shows a very small recovery of the SH annual mean sea ice cover in the second half of the 21st century in the low-end scenario SSP1-1.9 in both the NINT and OMA

configurations, by 6% and 3%, respectively. In another low end scenario SSP1-2.6, the recovery of the SH annual sea ice cover is simulated only in the NINT E2.1-G model while the OMA E2.1-G model produces continued decrease of the sea ice over both the high-latitude Northern and Southern oceans. E2.1-H model simulates strong decrease of the sea cover in all scenarios. Due to steeper surface warming (Table 1), the SH sea ice melt is much larger in all scenarios compared to the E2.1-G model (Table 2).

Comparison of the variability and relationships between the 20-year (2040-2059) annual mean of global surface air temperature and the 20-year (2040-2059) annual, March, and September means for the NH and SH sea ice are presented in Figure 6. For the Northern Hemisphere, the sensitivity of the sea ice to global warming (defined as the slope of the regression line) is the largest for September in both E2.1-G (-1.21×10^6 km^2/°C) and E2.1-H models (-0.94×10^6 km^2/°C) (Fig. 6e), which is consistent with the observed extreme shrinkage of the Arctic ice in September over the last years [*Stroeve and Notz,* 2015]. The E2.1-H models simulate strong sensitivities of the SH sea ice for the annual mean (-1.11×10^6 km^2/°C) and September mean (-1.48×10^6 km^2/°C) ice cover (Fig. 6b and 6f). Starting with the last decades of the historical simulations, the E2.1-H models continue the fast decline of the SH sea ice in all SSP emission scenarios (Fig. 6b, 6d, 6f). The SH sea ice loss is cited by *Miller et al.* [2021] as unrealistically large over the last decades of the historical simulations in the E2.1-H models. The E2.1-H models simulate stronger warming over the Southern Ocean compared to E2.1-G models for the historical period (Fig. 12 in *Miller et al.*, 2021) and for the SSP emission scenarios. In Section 5, Fig. 11b demonstrates warmer temperatures over high Southern latitudes in the E2.1-H model for the last two decades of the SSP2-4.5 scenario.

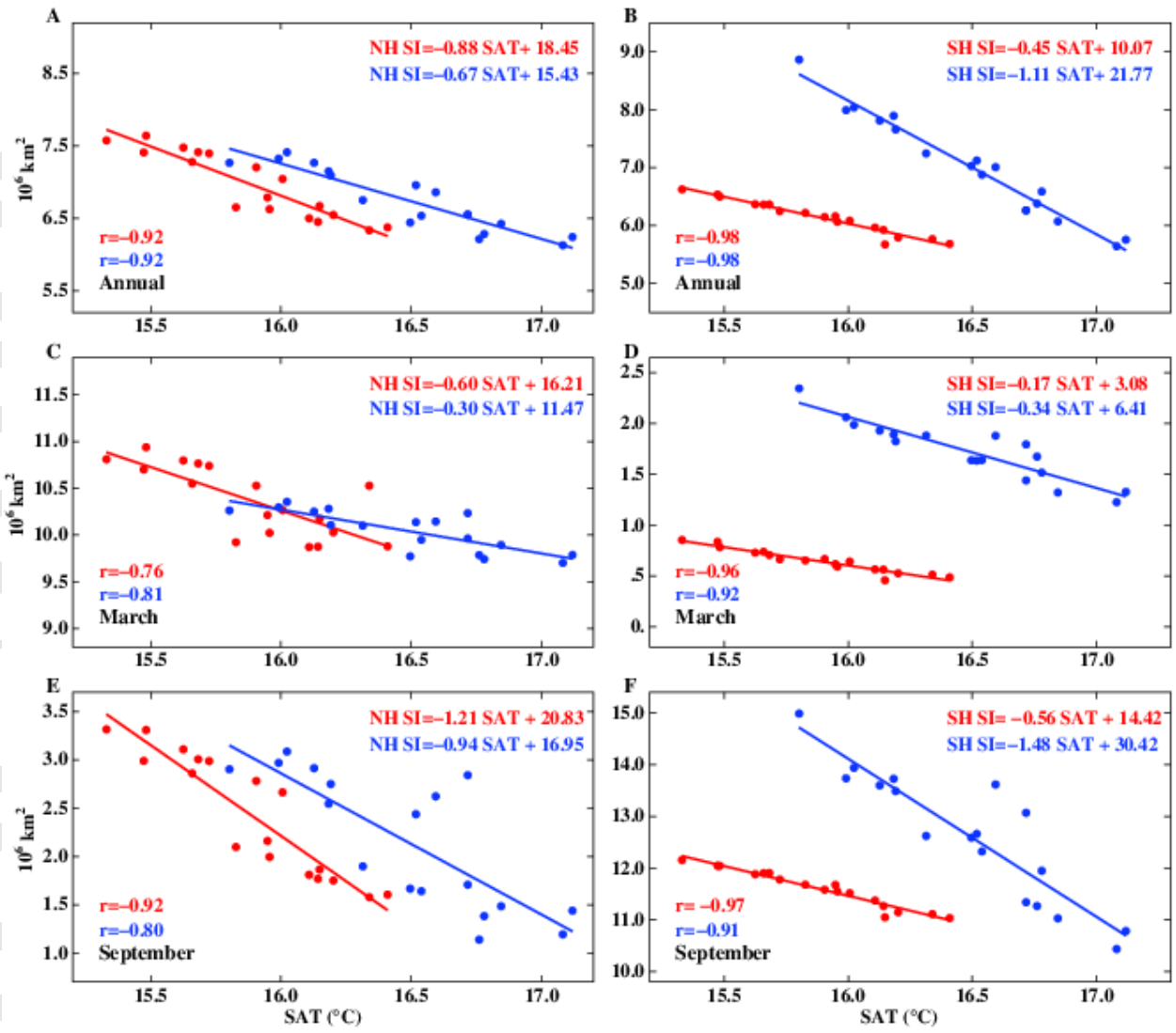

Figure 6. Relationship between the 20-year (2040-2059) annual mean of global surface air temperature and sea ice area (10^6 km^2). (A) 20-year (2040-2059) annual mean of Northern Hemisphere sea ice area; (B) 20-year (2040-2059) annual mean of Southern Hemisphere sea ice area; (C) 20-year (2040-2059) March mean of Northern Hemisphere sea ice area; (D) 20-year (2040-2059) March mean of Southern Hemisphere sea ice area; (E) 20-year (2040-2059) September mean of Northern Hemisphere sea ice area; (F) 20-year (2040-2059) September mean of Southern Hemisphere sea ice area. Red dots are for E2.1-G models, blue dots are for E2.1-H models.

For all seasonal means, the sensitivities of sea ice to global warming is stronger over the SH than over the NH in the E2.1-H models. Furthermore, over the Southern Ocean the sensitivities of the sea ice to global warming are stronger at least by factor of two in the E2.1-H models compared to the E2.1-G models (Fig. 6b, 6d, 6f). Over the NH, the sensitivities of the sea ice cover to surface air temperature are comparable in both models for annual mean and summer season (Fig. 6a, 6e) while for winter season sensitivity is much weaker in the E2.1-H models (Fig. 6c). In general, the cold season Arctic sea ice cover is much less sensitive to the change in the annual mean surface air temperature in both models (Fig. 6c, 6e).

Analyzing declines of the NH summer sea ice cover below 1×10^6 km^2, a commonly used threshold for a seasonably ice-free Arctic, the GISS-E2.1 models simulate much larger sea ice coverage for the last decades of the historical period compared to CMIP5 versions. For the middle 21st century (2040-2059), the almost ice-free summer Arctic conditions are produced by the E2.1-H models in the intermediate scenario SSP4-6.0 and in the high-end scenarios SSP3-7.0 and SSP5-8.5 (Fig. 6e). The E2.1-G models simulate the ice-free summer Arctic at the end of the 21st century in these high-end scenarios. The middle 21st century surface temperature warming of +1.0 to +1.6°C relative to the last decade of the historical period is required in the E2.1-H models to produce this summer ice-free Arctic (Table 1). For the E2.1-G models, the end 21st century surface warming of +1.9 to +3.8°C is shown for the ice-free summer Arctic (Table 1). This surface temperature increase for ice-free conditions is larger compared to CMIP5 versions because simulated sea ice area at the end of the historical time period**,** that is used as initial conditions for all future scenarios, is greater in the GISS-E2.1 models [*Miller et al.*, 2021].

4.3. Ocean Heat Content and Thermosteric Sea Level Changes

The ocean is the largest energy collector on Earth. It absorbs most of the excess heat trapped by greenhouse gases, leading to rising ocean temperatures and to increasing ocean heat content. Over the historical simulations, the E2.1-H models take up more ocean heat for both NINT and OMA configurations with the largest heat uptake in E2.1-H OMA ensemble matching the estimated column uptake from observations [*Zanna et al.,* 2019]. Both CMIP6 E2.1-G and E2.1-H models show markedly smaller heat uptake over the 20th century than the CMIP5 GISS coupled models [*Miller et al.*, 2021].

Both GISS CMIP6 models simulate a similar ocean warming following the starting year of the future experiments, 2015. Overall, the OMA versions for both models show slightly larger increases in the ocean heat content (Table 3) that follows stronger ocean heat uptake for the last two decades (1995-2014) of the historical period (Fig. 19 in *Miller et al.*, 2021) in the OMA configurations in general. The largest increases in ocean heat content from 2015 to 2100 are seen in the SSP5-8.5, with increases of 9-10% relative to the year 2015 in both the E2.1-G and E2.1-H models. This warming is close to GISS CMIP5 RCP8.5 ocean heat content increase over the 21st century (relative to the year 2006 ocean heat content, the starting year of all CMIP5 RCP experiments). In another high-end scenario SSP3-7.0, the ocean warming is 8-9% in both models. The lowest ocean warming between 4 and 5% is simulated in both low-end scenarios SSP1-1.9 and SSP1-2.6, which is similar to CMIP5 RCP2.6 warming. For the intermediate SSP2-4.5 and SSP4-6.0 scenarios, predicted ocean warming is between 7 and 8% for both CMIP6 coupled models.

Table 3. Ocean heat content change (10^{22} J) in 2100 relative to 2015.

	E2.1-H		E2.1-G	
	NINT	**OMA**	**NINT**	**OMA**
SSP1-1.9	102	110	115±2.7	128
SSP1-2.6	118±1.7	130	136±0.8	146±1.7
SSP4-3.4	133	143	146±1.0	158
SSP2-4.5	156±1.8	164±1.8	172±1.9	180±2.3
SSP4-6.0	171	185	184±3.0	198
SSP3-7.0	189±1.9	210	202±1.6	222±2.2
SSP3-7.0LOW	180	196	196±1.9	211
SSP5-8.5	231±1.1	241±2.1	248±2.3	259±1.3
SSP5-3.4 OS	143±1.6	154	159±2.6	172±1.5

The expansion of ocean volume due to warming, so-called thermosteric sea level rise, increases throughout the 21st century in all scenarios relative to the last decade of the historical simulations (Table 4). Over the historical period, 1850-2014, the thermosteric sea level rise is about 2 and 4 cm for the E2.1-G and E2.1-H models, respectively [*Miller et al.*, 2021] that is

comparable to observational estimates since 1961 [Church et al., 2011]. The rate of the global mean thermosteric sea level rise is 5-10% is larger in the E2.1-G than in the E2.1-H models (Table 4) that is consistent with a stronger ocean heat uptake in the E2.1-G models for all future scenarios (Table 3). There is greater thermosteric sea level rise in the OMA configuration for both ocean models due to larger ocean warming (Table 3). Comparing sea level at 2100 to the historical last-decade mean sea level, the thermosteric sea level rises are the largest for the high-end scenario SSP5-8.5. They are almost double the thermosteric sea level increases of the low-end scenario SSP1-1.9, which are 14-18 cm for the SSP1-1.9 and 30-33 cm for the SSP5-8.5. The CMIP6 scenarios SSP1-2.6, SSP2-4.5, SSP4-6.0, and SSP5-8.5 simulate about the same thermosteric sea level rise as in the analogous CMIP5 RCP2.6, RCP4.5, RCP6.0, and RCP8.5 scenarios (Table 3 from *Nazarenko et al.* [2015]) for the NINT E2.1 model configuration. The thermosteric sea level rises in the SSP5-8.5, SSP2-4.5, and SSP1-2.6 are close to the reported global mean thermal expansions for the CMIP6 ensemble mean of 20 models [*Hermans et al.*, 2021].

Table 4. Global Thermosteric Sea Level Rise (m) in 2100 relative to (2005-2014) mean sea level.

	E2.1-G		**E2.1-H**	
	NINT	**OMA**	**NINT**	**OMA**
SSP1-1.9	0.16±0.01	0.18	0.14	0.16
SSP1-2.6	0.18±0.01	0.20±0.01	0.16±0.01	0.19
SSP4-3.4	0.20±0.01	0.22	0.17	0.19

SSP2-4.5	0.22±0.01	0.24±0.01	0.21±0.01	0.23±0.01
SSP4-6.0	0.23±0.01	0.25	0.22	0.25
SSP3-7.0	0.25±0.01	0.28±0.01	0.24±0.01	0.28
SSP3-7.0LOW	0.24±0.01	0.27	0.22	0.26
SSP5-8.5	0.30±0.01	0.32±0.0	0.30±0.01	0.33±0.01
SSP5-3.4OS	0.21±0.01	0.23±0.01	0.19±0.01	0.21

Warming has a strong impact on the North Atlantic deep water formation that in turn affects the strength of the meridional overturning circulation. The weakening of the North Atlantic overturning originates from reduction of surface ocean salinity as a result of the freshwater flux from the sea ice melt under warming conditions. The recovery of the overturning starts with the further ocean warming in low and middle latitudes and increasing the density contrast between sinking and rising regions of the North Atlantic. The processes of thermohaline circulation weakening and recovery as function of timescale, magnitude of forcing and representation of key ocean processes are presented and extensively discussed in *Manabe and Stouffer* [1999] as well as in *Manabe and Stouffer* [1994].

The E2.1-G models simulate a tendency of stronger declines of the overturning circulation in historical experiments compared to E2.1-H (Fig. 21 from *Miller et al.* [2021]). This tendency of the overturning weakening continues in the SSP experiments, which is consistent with the strong and significant linear relationship between mean present-day overturning strength and projected 21st century overturning decline shown by *Weijer et al.* [2020]. Figure 7 shows the Atlantic overturning circulation at 26°N for the E2.1-G models. The largest decrease of 56-65% in the 21st century overturning stream function relative to the last decade of the historical simulation is produced in the warmest scenario SSP5-8.5 in the E2.1-G models. This weakening of the Atlantic overturning is comparable to the stream function reduction in the similar CMIP5 RCP8.5 (Fig. 15a from *Nazarenko et al.* [2015]). However, both SSP2-4.5 and SSP4-6.0 show stronger decreases in the 21st century overturning circulation, 35-55%, compared to the analogous CMIP5 RCP4.5 and RCP6.0 (35-45%) [*Nazarenko et al.*, 2015]. Although both low-end scenarios SSP1-1.9 and SSP1-2.6 also simulate large reductions of the overturning (9-37%), there is a sign of slow increase and recovery of the Atlantic overturning by the end of the 21st century (Fig. 7a). Figure 7c demonstrates a recovery of the Atlantic overturning in the overshoot scenario SSP5-3.4OS that follows a strong reduction of energy imbalance in SSP5-3.4OS over the second half of the 21st century (Fig. 5c).

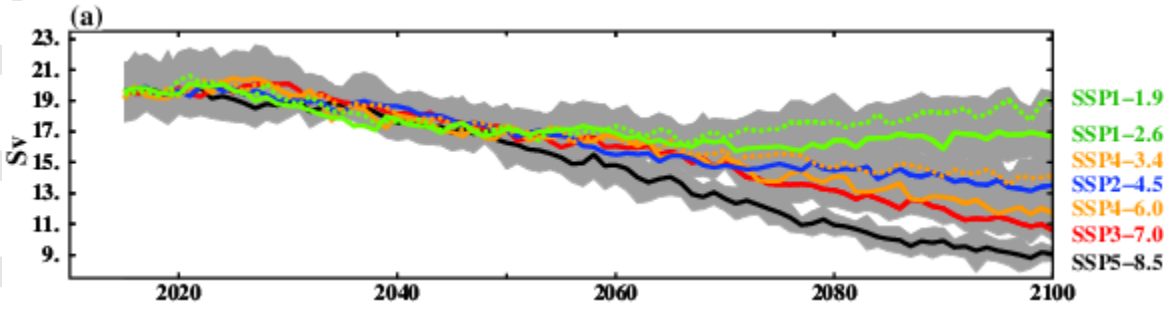

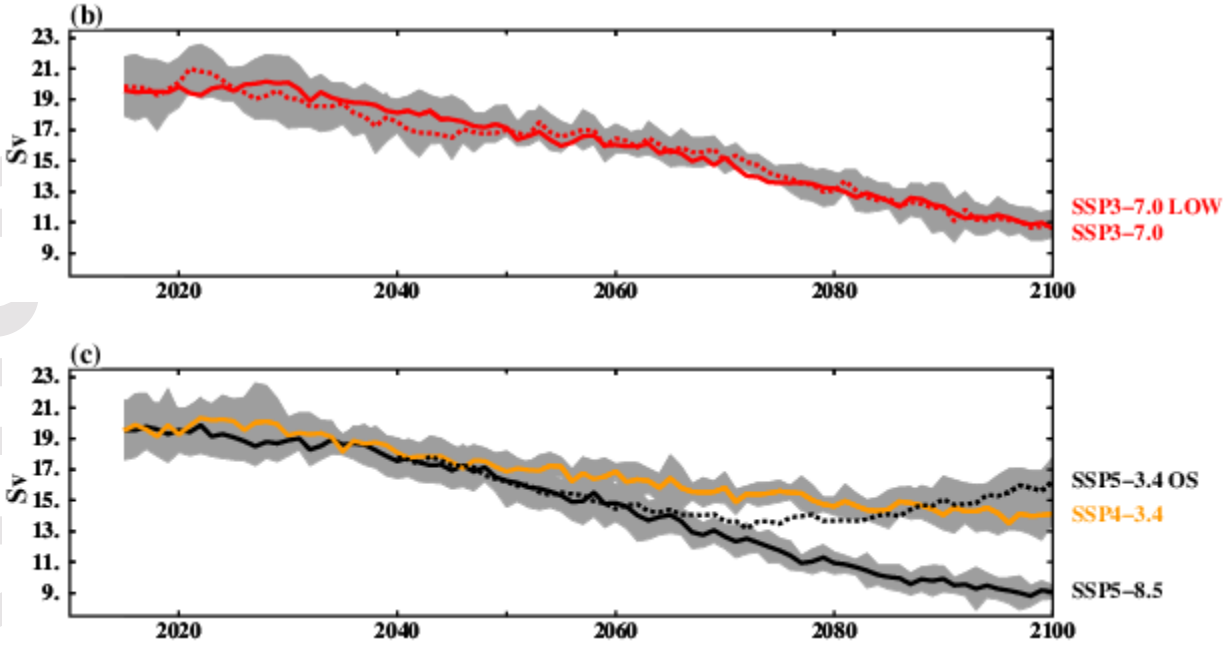

Figure 7. North Atlantic overturning stream function at 26°N (Sverdrup). The data were averaged for the NINT and OMA E2.1-G models.

Figure 8 shows the Atlantic overturning circulation at 26°N for the E2.1-H models. The E2.1-H models produce a smaller reduction in the overturning stream function over the 21st century that shows a continuation of slow weakening in the North Atlantic overturning from the historical simulations (Fig. 21 from *Miller et al.* [2021]). For the high-end scenario SSP5-8.5, the decrease in overturning is between 49 and 56% relative to the last decade of the historical simulation. The E2.1-H models show no sign for the recovery of the overturning circulation in the low-end scenarios SSP1-1.9 and SSP1-2.6 over the last decades of the 21st century (Fig. 8a). This overturning slowdown with no recovery in the E2.1-H models is similar to the overturning behavior in the CMIP5 E2-H versions (Fig. 15b from *Nazarenko et al.* [2015]). In the overshoot scenario SSP5-3.4OS, there is a slowdown in the overturning weakening over the second half of the 21st century (Fig. 8c) with the sign of equilibrium state (about 60% of the overturning over the last decade of the historical simulation).

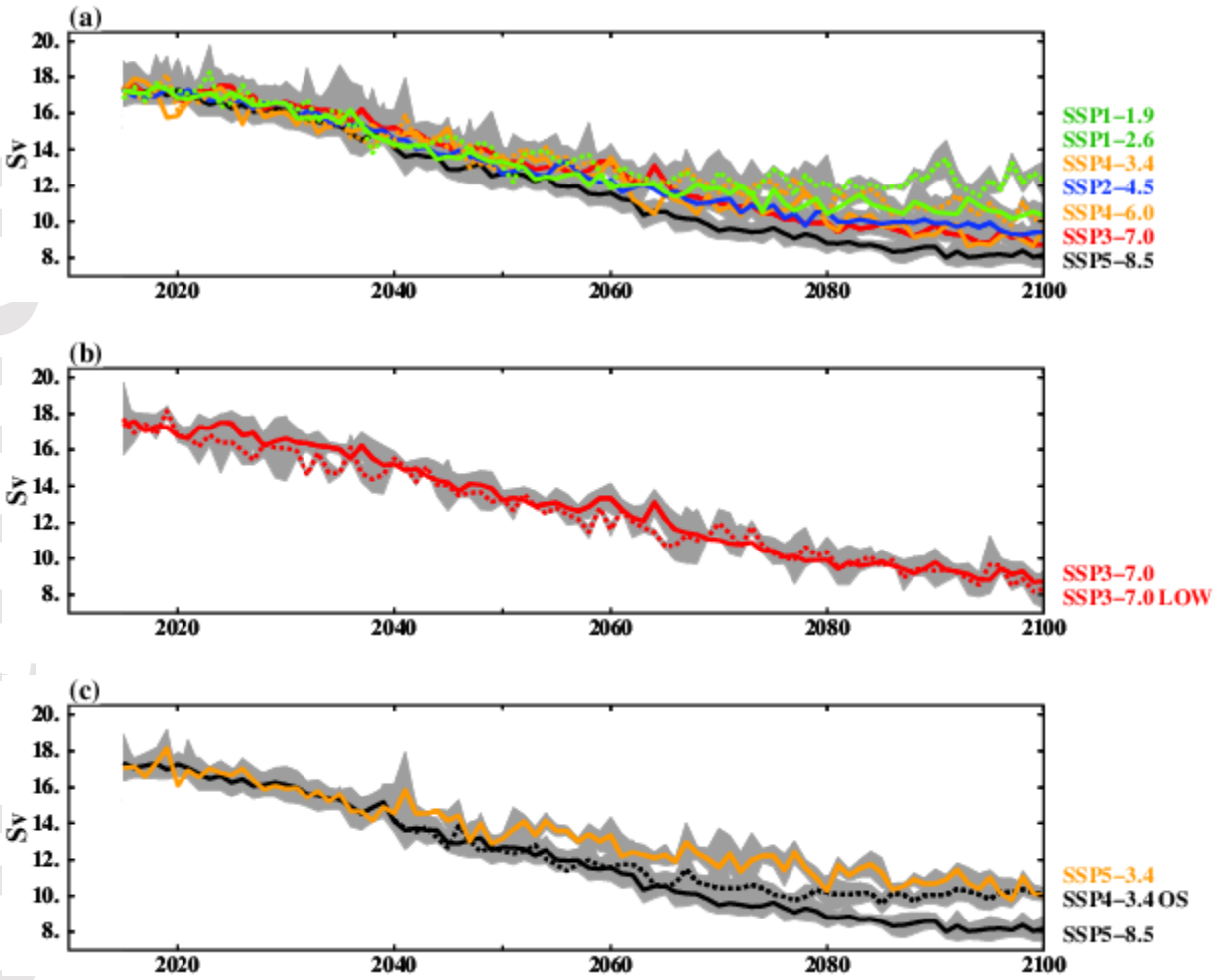

Figure 8. The same as Fig. 7 but for the E2.1-H models.

Figure 9 presents the sensitivity of the North Atlantic meridional overturning circulations to the change of the global annual mean surface air temperature for each SSP experiment and all coupled model configurations. The changes of both the North Atlantic overturning and surface air temperature are taken for the last decade of the 21st century 2091-2100 minus the last decade of the historical simulation 2005-2014. The correlation between the overturning and surface air temperature is stronger in the E2.1-H models although the overturning decline is larger in the E2.1-G models (red symbols and red linear trend line for E2.1-G versus blue symbols and blue linear trend line for E2.1-H). The sensitivity of the overturning circulation to the warming is much stronger in the E2.1-G models with the tendency of the complete shutdown of the convective

processes and deep-water formation in the warm scenarios SSP5-8.5, SSP3-7.0 and SSP4-6.0. The overturning circulation in the E2.1-H model shows slowdown in half in the warmest scenario SSP5-8.5 with the stabilizing tendency at this value.

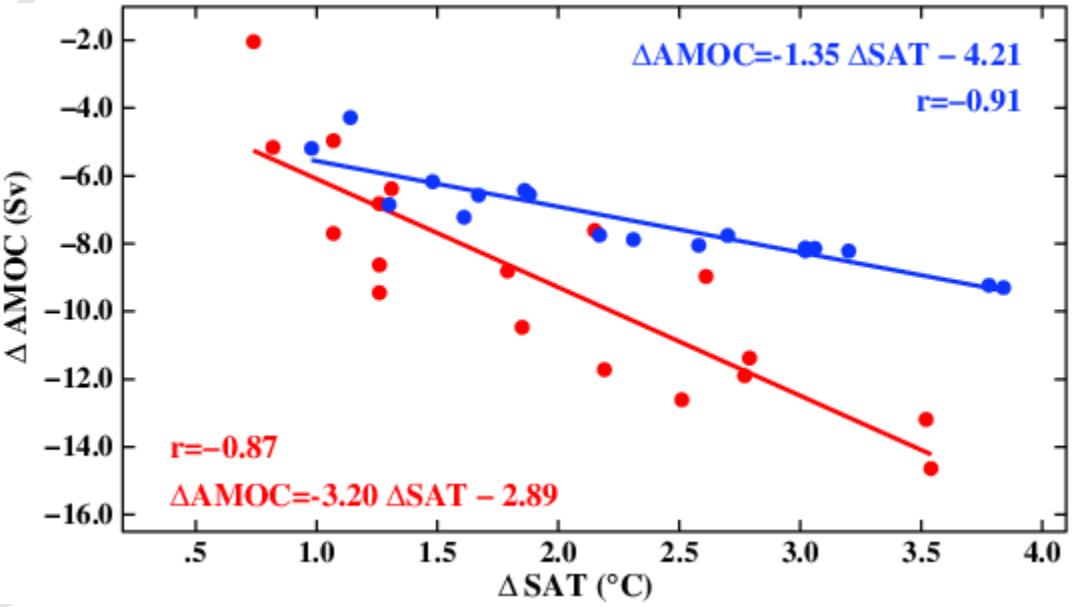

Figure 9. Relationship between the surface air temperature difference and the North Atlantic meridional overturning circulation for the last 21st century decade 2091-2100 minus 2005-2014. The red symbols are for SSP experiments with the E2.1-G model; the blue symbols are for the E2.1-H models.

Stronger decline of the overturning circulation in the CMIP6 ScenarioMIP scenarios relative to the CMIP5 future projections was reported by *Weijer et al.* [2020] with pronounced difference for the scenarios with weakest radiative forcing. The CMIP6 multimodel mean decrease of the overturning is projected as 24%, 29%, 32%, and 39% for SSP1-2.6, SSP2-4.5, SSP3-7.0, and SSP5-8.5, respectively [*Weijer et al.*, 2020]. For the GISS-E2.1 model configurations, the range of the overturning decline is between 17-37%, 34-49%, 40-55%, and 48-56% for the respective SSP emission scenarios in different E2.1 model configurations. The overturning

decrease in the E2.1 model is stronger than the reported decline in the CMIP6 models for the medium and high-end scenarios, and it is comparable for the low-end scenario SSP1-2.6. The overturning slowdown in the SSP1-2.6 is at least two times stronger than in the analogous CMIP5 RCP2.6 scenario that is in line with the analysis of *Weijer et al.* [2020].

5. Regional changes of surface air temperature and precipitation

The geographical distributions of surface air temperature change for the last twenty years of the 21st *century* (2081-2100) relative to the last twenty years (1995-2014) of the corresponding historical simulation are shown in Fig. 10 for four selected scenarios, SSP1-2.6, SSP2-4.5, SSP4-6.0, and SSP5-8.5. In this figure, the temperature changes are averaged over the NINT E2.1-G and E2.1-H climate models for each SSP emission scenario. The regional difference between OMA and NINT, and E2.1-H and E2.1-G are presented separately to demonstrate the distinctions between them (Fig. 11). The number above the upper right corner is the global mean temperature change.

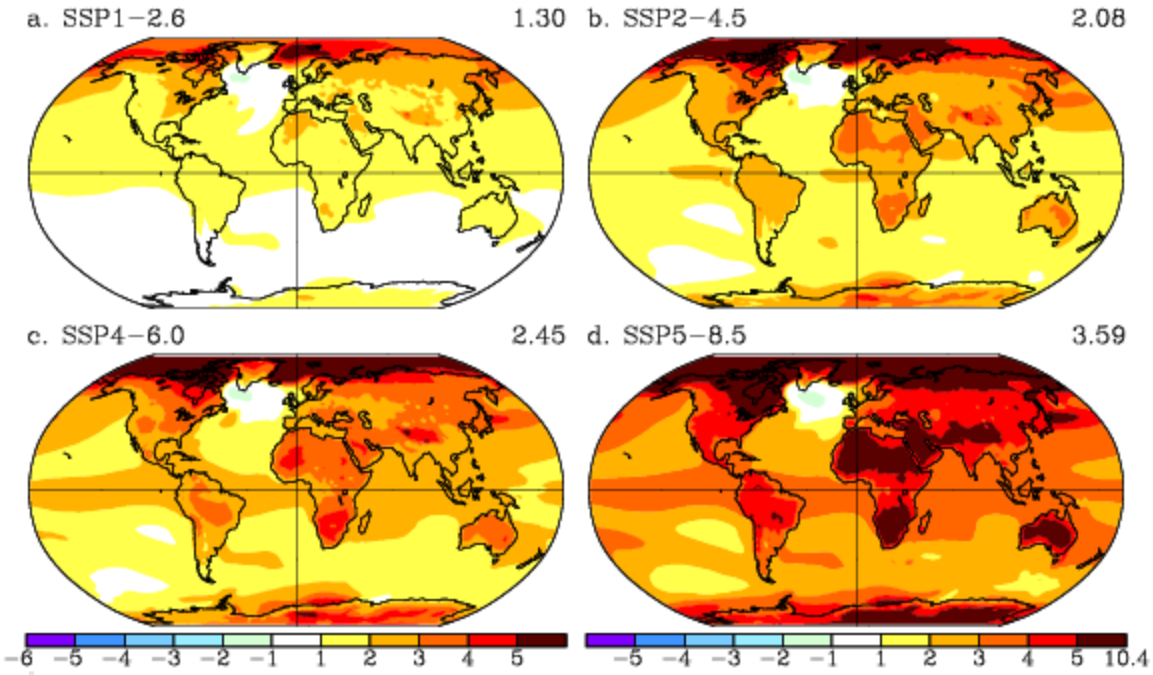

Figure 10. Surface air temperature differences (°C) for late 21st century 2081-2100 minus 1995-2014 of the corresponding historical ensemble member for the NINT climate model. (a) SSP1-2.6; (b) SSP2-4.5; (c) SSP4-6.0; (d) SSP5-8.5.

The specific regional patterns of the surface air temperature changes, such as polar amplification and greater warming over land than over the ocean, are the same as those simulated with previous GISS climate model versions [*Schmidt et al.*, 2014; *Miller et al.*, 2014; *Nazarenko et al.*, 2015] and other models [*Tebaldi et al.*, 2021*; Tokarska et al.*, 2020]. The geographical patterns of warming are similar in all scenarios (Fig. 10). Scenarios SSP1-2.6 and SSP2-4.5 show stronger temperature increases over the northern hemisphere than over the Southern Hemisphere (Fig. 10a and 10b). Scenarios SSP4-6.0 and SSP5-8.5 simulate larger and more uniformly spread warming over both hemispheres with much stronger and more area-covered Arctic amplification (Fig. 10c and 10d). A small area of surface temperature cooling of about -1°C is produced over

the North Atlantic to the south of Greenland in all scenarios. This region is the Northern section of the North Atlantic meridional overturning circulation with strong vertical convection.

Comparison of the GISS-E2.1 late-21st century surface warming temperature change to the same time interval for the GISS-E2 CMIP5 simulations (relative to the 1986-2005 average), shows that the E2.1 surface warming is greater for all scenarios. The largest difference in the late-21st century warming relative to 1986-2005 is simulated for the low-end scenario SSP1-2.6, which is about 2 times stronger on average than for the CMIP5 RCP2.6. Three other selected scenarios, SSP2-4.5, SSP4-6.0, and SSP5-8.5, show the warming of about 1°C greater around the globe.

Figure 11 demonstrates differences of ensemble mean surface air temperature change for the late 21st century 2081-2100 minus 1995-2014 across different model configurations for the SSP2-4.5 scenario. In this plot, the temperatures are averaged over both the E2.1-G and E2.1-H simulations. Fig. 11a shows that the OMA atmospheric model simulates stronger warming over the large area of the SH and cooler temperatures over the NH. The area-integrated relative cooling over the Northern latitudes is stronger giving negative global changes in the OMA model (Table 1). This is opposite to the temperature response in the CMIP5 GISS-E2 TCADI (OMA) model (Fig. 7a from *Nazarenko et al.*, 2015). The CMIP5 OMA model simulated warmer temperatures relative to the CMIP5 GISS-E2 NINT model. Different response of climate in the NINT and OMA models for the ScenarioMIP scenarios is going to be covered separately and presented in another research study.

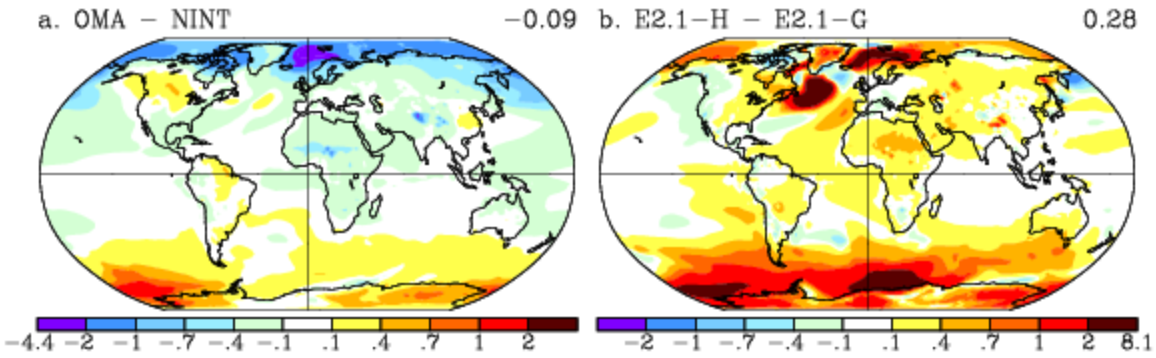

Figure 11. Differences of surface air temperature change, 2081-2100 minus 1995-2014, (°C) in different climate models for the SSP2-4.5 scenario. (a) OMA – NINT; (b) E2.1-H – E2.1-G.

The E2.1-H model produces much greater warming over both northern and southern high latitudes compared to E2.1-G (Fig. 11b), associated with less mixing of heat to the deep ocean and greater decrease of sea ice cover [*Miller et al.*, 2021]. Greater warming in the E2.1-H model is also seen for the global mean surface temperature change in the SSP2-4.5 scenario (Table 1). The absence of the cooling near the Labrador Sea in the E2.1-H model (Fig. 11b) leads to a smaller slowdown of the North Atlantic overturning compared to the E2.1-G model. Comparison of the difference between the E2.1-H and E2.1-G models to the difference of the CMIP5 model versions shows that the E2.1-H simulates more warming over the Southern Ocean and less warming over high latitudes in the Northern hemisphere.

Figure 12a shows the surface air temperature change for 2081-2100 relative to 1995-2014, normalized by the change in the annual global mean surface temperature for the NINT E2.1-G climate model in the scenario SSP2-4.5. Such normalization allows us to see regional responses in different model configurations and SSP emission scenarios. There is stronger warming over the

Northern polar region in the E2.1-H model (Fig. 12b) that leads to more extensive sea ice melt in the high northern latitudes (Table 2). Stronger warming over tropics and southern Atlantic compared to the temperatures over the North Atlantic in the SSP5-8.5 **(**Fig. 12c**)** is caused by weakening of the Atlantic meridional overturning circulation and reduced ocean heat transport from low tropical latitudes to the north in the SSP5-8.5.

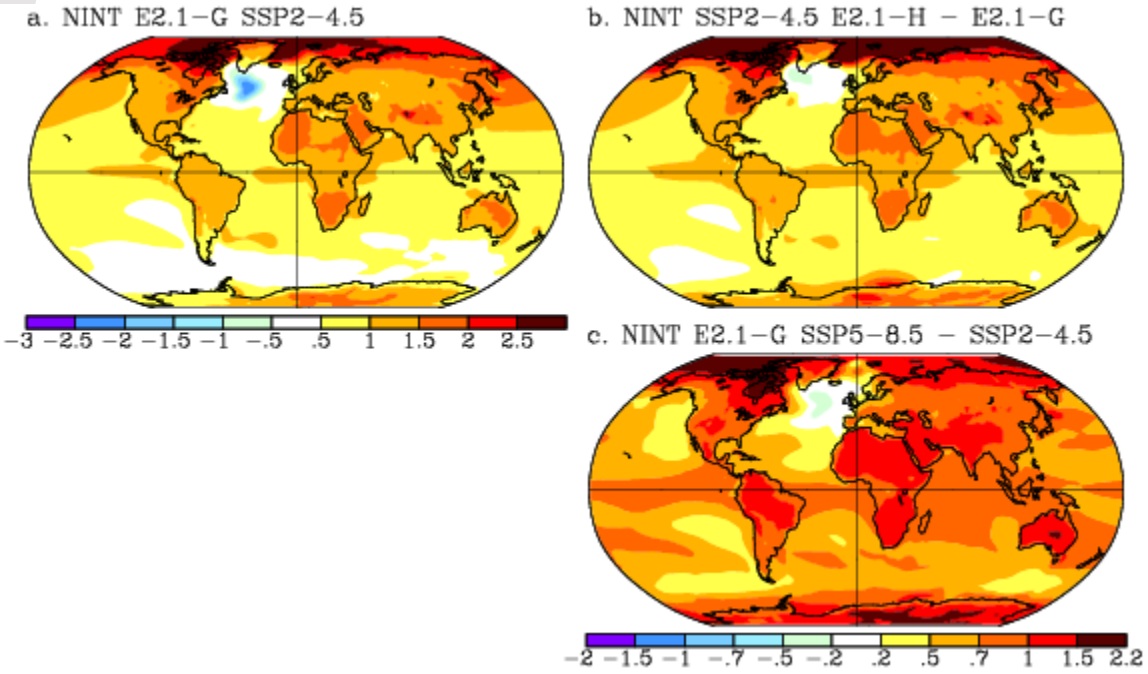

Figure 12. Surface air temperature change for 2081-2100 minus 1995-2014 of the corresponding historical ensemble member of the climate model, normalized by the change in the annual global mean surface temperature for the NINT E2.1-G SSP2-4.5. (a) NINT E2.1-G SSP2-4.5; (b) NINT SSP2-4.5 E2.1-H - E2.1-G; (c) NINT E2.1-G SSP5-8.5 - SSP2-4.5.

Figure 13 shows the geographical patterns of precipitation. Following the increases in surface air temperature, the changes in precipitation are the smallest in the SSP1-2.6 (Fig. 13a) and the largest in the SSP5-8.5 (Fig. 13d). Precipitation increases along the Pacific Intertropical

Convergence Zone and along the equatorial ocean areas and decreases over much of the subtropics, which is the effect of more moisture convergence in the regions with already strong moisture convergence [*Held and Soden*, 2006; *Stevens et al.*, 2013]. The enhanced poleward transport of moisture arising from the higher specific humidity in a warmer climate results in the increases of precipitation in the middle and high latitudes that is also reported for all future scenarios by *Held and Soden* [2006] and *Tebaldi et al.* [2021].

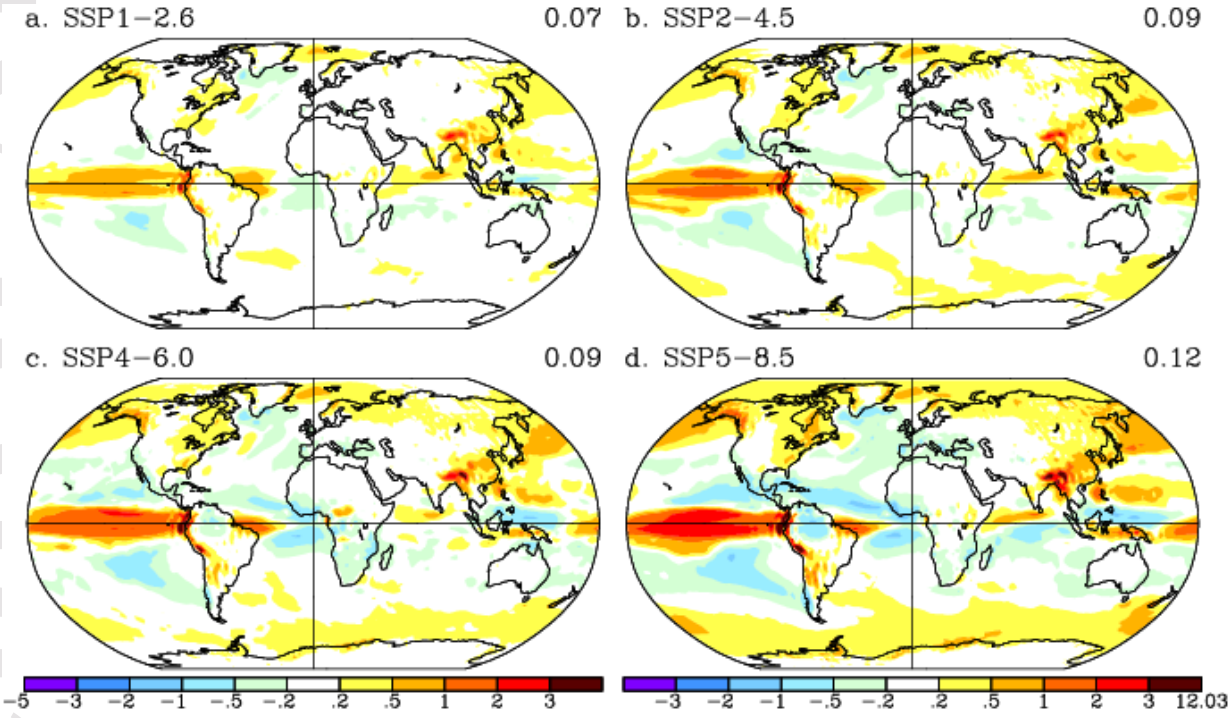

Figure 13. Precipitation differences (mm/d) for late 21st century 2081-2100 minus 1995-2014 of the corresponding historical ensemble member for the NINT climate model. (a) SSP1-2.6; (b) SSP2-4.5; (c) SSP4-6.0; (d) SSP5-8.5.

The comparison of the late 21st century precipitation changes to the last twenty years of the CMIP5 historical simulation, 1986-2005, shows larger precipitation increases for the SSP1-2.6

and SSP2-4.5 following stronger warming than in the same CMIP5 RCP2.6 and RCP4.5. In the SSP4-6.0 and SSP5-8.5 scenarios, the regions of increased and decreased precipitation changes are larger as well as the maximum and minimum of precipitation although the global mean precipitation changes are the same as for CMIP5 RCP6.0 and RCP8.5 [*Nazarenko et al.*, 2015].

Analysis of precipitation change for the SSP2-4.5 scenario demonstrates that the climate models with interactive chemistry and aerosols OMA produce more rainfall change in equatorial ocean areas and over the Intertropical Convergence Zone compared to the model with non-interactive (NINT) aerosol chemistry (Fig. 14a). The Amazon Basin and the subtropical ocean regions show increasing drying when the interactive aerosol chemistry is added to the atmospheric model. There is increased precipitation over the tropical and subtropical ocean areas, over the North Atlantic and over the Southern Ocean in the E2.1-H model relative to the E2.1-G model (Fig. 14b) due to stronger warming over these areas in the E2.1-H model (Fig. 11b).

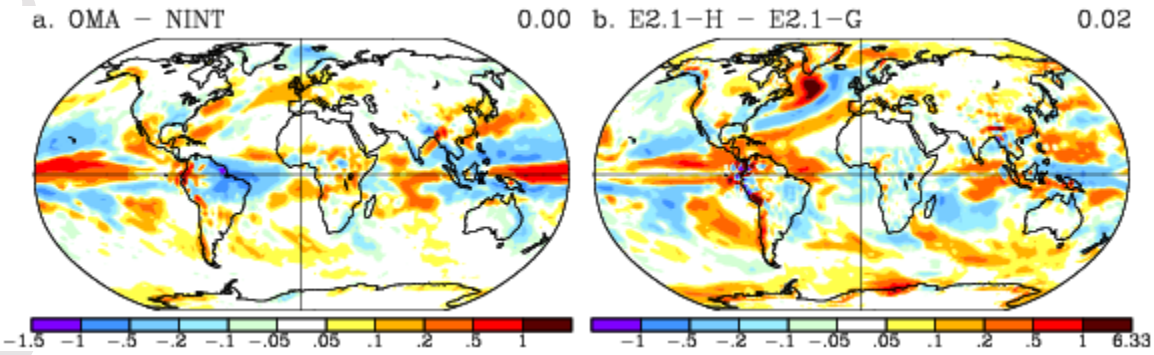

Figure 14. Differences of precipitation change, 2081-2100 minus 1995-2014, (mm/d) in different climate models for the SSP2-4.5 scenario. (a) OMA – NINT; (b) E2.1-H – E2.1-G.

6. Projections of the Extratropical Circulation

The annular modes, near-zonally symmetric patterns of pressure centered over the poles of each hemisphere and extending from the surface to the lower stratosphere, represent the largest interannual variability in the present-day extratropical circulation [*Thompson and Wallace,* 2000; *Baldwin and Dunkerton,* 2001]. Figure 15 shows projections of sea-level pressure change over the CMIP6 historical period and into the future according to the SSP2-4.5 and SSP5-8.5 scenarios. Each plot shows the annular index, defined as the leading principal component (PC) of sea-level pressure (SLP) in each hemisphere and its evolution between 1850 and 2100. (Differences between the scenarios by year-2100 increase in the subsequent century as the CO_2 concentration continues to rise in SSP5-8.5.) During the NCEP reanalysis period (1948-2020), the NH annular mode accounts for 22% of interannual variations in NH wintertime SLP, compared to the range of 21 to 27% exhibited by the different model configurations. During the SH springtime, the observed annular variance is 40%, within the range of 33 -- 46% simulated with the GISS Ocean and 34 -- 42% simulated with HYCOM. The variance associated with the second leading mode in each hemisphere is far smaller (roughly 10%) and statistically well-separated. The annular patterns dominate not only present-day interannual variability in the extratropics but also the change in hemispheric pressure over the entire historical period and coming centuries.

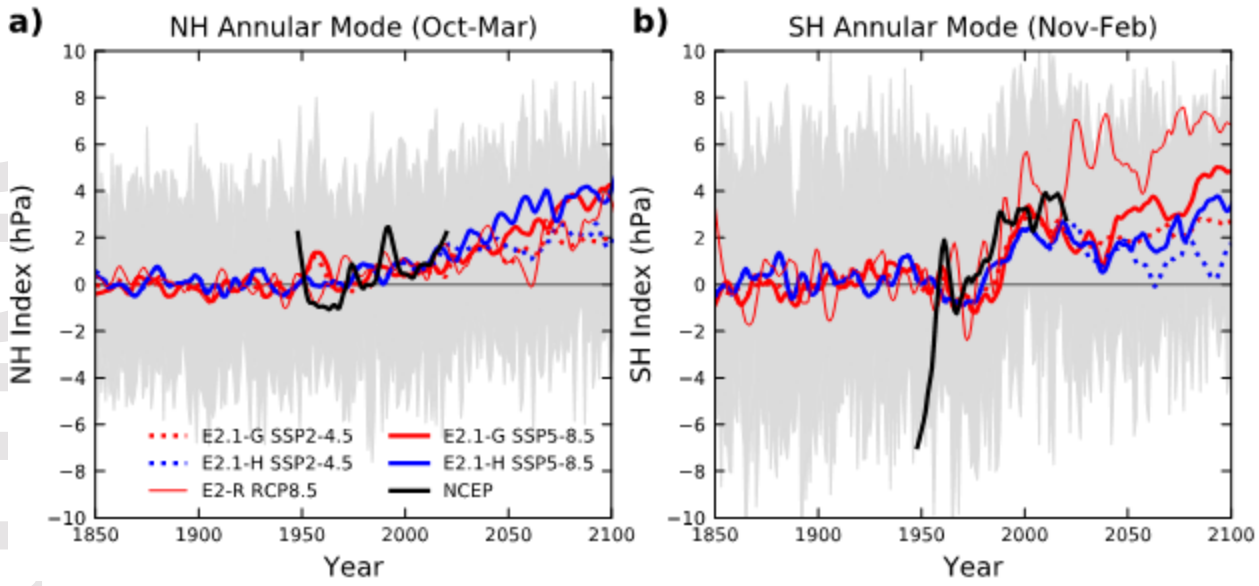

Figure 15. Annular mode index (hPa) corresponding to the leading a) NH winter (October to March) and b) SH spring (November to February) principal component (PC) during the historical period followed by SSP2-4.5 (dotted) and SSP5-8.5 (solid). The leading mode for the GISS-E2-R CMIP5 model version is also plotted (thin solid). Anomalies are defined relative to the period 1850 to 1970. The NINT model configuration is used for each calculation. The anomalous pressure is derived from the ensemble average of the leading PC between 1850 and 2300 (2500 for SSP2-4.5). The mean pressure anomaly poleward of 60° N is given by the PC index but with opposite sign. Pressure is smoothed using a lowess filter with a 10-year window; Gray shading shows the unsmoothed intra-ensemble range of pressure variations for the GISS-E2.1-G NINT f2 ensemble under the SSP2-4.5 scenario. The leading annular PC of NCEP reanalysis SLP is adjusted to match the average of this ensemble during the period 1948-2020 (black line).

During NH winter (October to March), the annular index shows a steady increase over the 21st century, corresponding to a steady decrease of Arctic sea-level pressure. The change is twice as large for the SSP5-8.5 scenario compared to SSP2-4.5, consistent with the larger increase in GHG radiative forcing associated with the former. Arctic pressure in the SSP5-8.5 scenario continues to decrease over the twenty-second century as GHG concentrations rise [*Meinhausen et al.*, 2020]. NH annular trends are larger in GISS-E2.1-G compared to its CMIP5 predecessor, despite smaller radiative forcing by GHGs in the former. The annular response is similar among the ensembles with different ocean configurations. Despite the clear ensemble-mean trend during the **21st** century, annular variability among the ensemble members is large suggesting that observed trends may not be clearly distinguishable even by 2100.

In SH spring (November to February), changes are again higher under the SSP5-8.5 scenario. Ozone variations are important additional drivers of annular trends in this hemisphere (e.g. *Shindell and Schmidt,* 2004); *Miller et al.* (2006) use the CMIP3 multimodel suite to attribute the abrupt decrease in observed Antarctic pressure at the end of the last (twentieth) century to ozone depletion. Figure 15b shows a temporary decline in the SH annular index early in this century coincident with the recovery of stratospheric ozone, before resuming an upward trend by 2100 as GHG concentrations continue to rise. In contrast to the NH, the GISS-E2.1-G SH annular trend is smaller than for its GISS-E2-R CMIP5 predecessor. For both SSP2-4.5 and SSP5-8.5, annular trends are larger when calculated in the HYCOM configuration than with the GISS ocean, in contrast to the insensitivity of NH trends with respect to the ocean configuration. This raises the question of how future differences in the Southern Ocean projected by the ocean configurations project onto the annular mode.

7. Conclusions

We describe the GISS-E2.1 response to forcing for the CMIP6 SSP future scenarios (2015–2100) using two atmospheric physics versions coupled to two different ocean models. The OMA version of the GISS-E2.1 model provides the atmospheric aerosols and ozone for the NINT version based on state-of-the-art "AMIP-style" OMA simulations. This gives a greater consistency between two atmospheric model versions. At the same time, the differences in response between the NINT and OMA versions could be more directly attributed to feedbacks between compositions and climate variations.

Two different ocean models coupled to the same atmospheric components allow us to see differences in specific behavior between E2.1-G and E2.1-H in response to the same scenario forcings. A larger fraction of heat uptake occurs near the ocean surface in the E2.1-H model compared to the E2.1-G configuration that was simulated for the historical period in the E2.1-H oceans [*Miller et al.*, 2020]. The tendency of the greater heat uptake confinement to the upper ocean in the E2.1-H models continues in all future scenarios that leads to stronger warming at the surface and mid-troposphere. Stronger warming of the surface temperatures over the high Northern and Southern latitudes leads to larger sea ice decrease in the E2.1-H configurations. Warmer temperatures near the Labrador Sea and the absence of atmospheric cooling leads to a smaller weakening of the Atlantic overturning in the E2.1-H models compared to the E2.1-G configurations.

Compared to CMIP5 GISS-E2 versions, the CMIP6 GISS-E2.1 climate model shows a stronger warming by 2100 in comparable scenarios SSP1-2.6, SSP2-4.5, SSP4-6.0, and SSP5-8.5 due to larger ECS and TCR. A proposed global threshold of "dangerous" climate change at 2°C relative to pre-industrial levels [*Meinshausen et al.,* 2009] continues to be the goal for the Paris

Agreement of limiting warming to below 2 or even 1.5°C [*Paris agreement*, 2015]. Two high-mitigation scenarios SSP1-1.9 and SSP1-2.6 maintain the surface warming below 2°C at the end of the 21st century relative to the pre-industrial surface temperature, except for the NINT E2.1-H model that allows warming of 2.2°C by 2100 for SSP1-2.6. In the latter model, there is a more rapid temperature increase with no sign of diminishing warming. The E2.1-G model shows a slow temperature decrease in the SSP1-2.6 extension to 2500 with a small recovery of Southern Ocean sea ice.

The overshoot scenario SSP5-3.4OS assumes reduced emission rates after 2040, reaching net negative emissions by the end of the century with the total effective forcings getting closer to the SSP1-2.6 effective forcings. The decrease of surface temperature in the second half of the 21st century and substantial cooling during the extension after 2100 illuminates how emission controls can moderate surface warming.

The intermediate scenario SSP2-4.5 shows different behavior of the Atlantic overturning circulation for the extension 2101-2500 in the NINT E2.1-G model. In eight out of ten ensemble members, the overturning circulation recovers to its value over the last decade of the historical period 2005-2014 after declining throughout the 21st century. The timing of recovery is different among these eight ensemble members. In the remaining two ensemble members, the overturning circulation completely collapses by 2350 and does not recover by the end of experiment extension to the year 2500. The analysis of the Atlantic overturning circulation for this scenario SSP2-4.5 in the NINT E2.1-G model will be presented elsewhere.

The E2.1-H model shows a much smaller decrease in the overturning circulation in all ScenarioMIP scenarios with no recovery even in two low-end scenarios SSP1-1.9 and SSP1-2.6 and no overturning collapse in either SSP2-4.5 or the high-end scenario SSP5-8.5. The changes in

the Atlantic overturning circulation are closely related to the upper ocean, where non-local salinity feedbacks restore and maintain the overturning stable in the E2.1-H models. We conclude that the North Atlantic response is a complicated function of timescale, magnitude of forcing and representation of key ocean processes. This wide range of responses is a key uncertainty in future climate projections.

Different regional patterns of warming in the NINT and OMA models lead to corresponding sea ice melt, precipitation changes and other climatic parameter variations. Stronger warming in the E2.1-H model is in most cases due to a large fraction of heat uptake near the ocean surface. Different model configurations allow us to quantify the resulting climate response, identify physical quantities that do not respond linearly, and assess where rates of change (as opposed to the change itself) appear to be important. More detailed analysis of aerosols, clouds, and their interactions and responses in the future projections of the E2.1 OMA model will be presented in the paper by Bauer et al. like the results for the historical simulations [*Bauer et al.*, 2020].

There are factors that are missing in the models, such as changes in vegetation, permafrost degradation (and the associated release of CO2 and methane), anomalous freshwater from the ice sheets [*Rye et al.*, 2020], and its impacts on the high latitude ocean changes. Changes of vegetation - both in composition and response of specific plant functional types - will change the surface response. Impacts of warming on ice sheets will impact their albedo, shape, extent and contributions to sea level rise beyond the thermosteric effects quantified here. Other composition-related feedbacks are also not included, for instance, permafrost degradation and its impacts on the high latitude carbon and methane cycles and changes in ocean marine bio-geo-chemical cycles (via changes in surface albedo, carbon cycling, dimethyl sulphide (DMS) and methane sulphonic

acid (MSA) emissions). Despite the missing processes noted above, future projections provide valuable information over a broad set of alternative scenarios. Plausible futures provide a relevant base for climate understanding, especially further assessment of possibility for low and high emission futures [*O'Neill et al.*, 2020].

One of the most important indicators of the severity of future warming impacts is the model climate sensitivity. Slightly larger climate sensitivities in the E2.1 model, both the effective and transient climate sensitivities, result in stronger warming than in the GISS CMIP5 scenarios comparable to SSP1-2.6, SSP2-4.5, SSP4-6.0, and SSP5-8.5. Stronger and wider range of warming, especially in high-end scenario SSP5-8.5, is confirmed in the CMIP6 simulations [*Tokarska et al.*, 2020; *Tebaldi et al.*, 2021]. It is attributable to the interplay of both higher ***ERFs*** by 2100 and higher climate sensitivities of the CMIP6 models [*Meehl et al.*, 2020; *Meinshausen et al.*, 2020; *Nicholls et al.*, 2020; *Seferian et al.*, 2020]. Understanding of this interconnection, as well as the uncertainty in the climate sensitivity, are useful for the assessment of future warming [*Sherwood et al.*, 2020].

Acknowledgements

Development of GISS-E2.1 was supported by the NASA Modeling, Analysis, and Prediction (MAP) Program. CMIP6 simulations with GISS-E2.1 were made possible by the NASA High-End Computing (HEC) Program through the NASA Center for Climate Simulation (NCCS) at Goddard Space Flight Center. We thank Ellen Salmon and the NCCS staff for hosting and providing convenient access to the model output. CMIP6 standard variables analyzed in this study are available through the Earth System Grid Federation and from https://portal.nccs.nasa.gov/datashare/giss_cmip6.

References

Bauer, S. E., K. Tsigaridis, G. Faluvegi, M. Kelley, K.K. Lo, R.L. Miller, and J. Wu (2020), Historical (1850–2014) aerosol evolution and role on climate forcing using the GISS ModelE2.1 contribution to CMIP6, *J. Adv. Model. Earth Syst.*, 12, e2019MS001978, doi:10.1029/2019MS001978

Baldwin, M. P., and T.J. Dunkerton (2001), Stratospheric harbingers of anomalous weather regimes. *Science*, 294**,** 581 - 584

Bleck, R. (2006), An oceanic general circulation model framed in hybrid isopycnic-cartesian Coordinates, *Ocean Modelling*, 4, 55-88.

Brennan, M. K., G.J. Hakim, and E. Blanchard-Wrigglesworth (2020), Arctic sea-ice variability during the instrumental era, *Geophys. Res. Let.*, 47, e2019GL086843, doi:10.1029/2019GL086843

Calvin, K., B. Bond-Lamberty, L. Clarke, J. Edmonds, J. Eom, C. Hartin, S. Kim, P. Kyle, R. Moss, H. McJeon, P. Patel, S. Smith, S. Waldhoff, and M. Wise (2017), SSP4: A world of inequality, *Global Environ. Change*, 42, 284-296, doi:10.1016/j.gloenvcha.2016.06.010

Church, J. A., N. J. White, L. F. Konikow, C. M. Domingues, J. G. Cogley, E. Rignot, J. M. Gregory, M. R. van den Broeke, A. J. Monaghan, and I. Velicogna (2011), Revisiting the Earth's sea-level and energy budgets from 1961 to 2008, *Geophys. Res. Lett.*, 38, L18601, doi:10.1029/2011GL048794

Clarke, L., J. Edmonds, V. Krey, R. Richels, S. Rose, and M. Tavoni (2009), International climate policy architectures: Overview of the EMF 22 International Scenarios, *Energ. Econ.*, 31, S64–S81

Fiedler, S., B. Stevens, M. Gidden, S.J. Smith, K. Riahi, and D. van Vuuren (2019), First forcing estimates from the future CMIP6 scenarios of anthropogenic aerosol optical properties and an associated Twomey effect, *Geosci. Model Dev.*, 12, 989–1007, doi:10.5194/gmd-12-989-2019

Fricko, O., P. Havlik, J. Rogelj, K. Riahi, Z. Klimont, M. Gusti, N. Johnson, P. Kolp, M. Strubegger, H. Valin, M. Amann, T. Ermolieva, N. Forsell, M. Herrero, C. Heyes, G. Kindermann, V. Krey, D.L. McCollum, M. Obersteiner, S. Pachauri, S. Rao, E. Schmid, W. Schoepp (2017), SSP2: a middle-of-the-road scenario for the 21st century**,** *Global Environ. Change*, 42, 251-267, doi:10.1016/j.gloenvcha.2016.06.004

Fujimori, S., T. Hasegawa, T. Masui, K. Takahashi, D. Silva Herran, H. Dai, Y. Hijioka, M. Kainuma (2017), AIM implementation of Shared Socioeconomic Pathways**,** *Global Environ. Change*, 42, 268-283, doi:10.1016/j.gloenvcha.2016.06.009

Gent, P.R., and J.C. McWilliams (1990), Isopycnal mixing in ocean circulation models, *J. Phys. Ocean*., 20, 150-155

Gidden, M. J., K. Riahi, S.J. Smith, S. Fujimori, G. Luderer, E. Kriegler, D.P. van Vuuren, M. van den Berg, L. Feng, D. Klein, K. Calvin, J.C. Doelman, S. Frank, O. Fricko, M. Harmsen, T. Hasegawa, P. Havlik, J. Hilaire, R. Hoesly, J. Horing, A. Popp, E. Stehfest, and K. Takahashi (2019), Global emissions pathways under different socioeconomic scenarios for use in CMIP6: a dataset of harmonized emissions trajectories through the end of the century, *Geosci. Model Dev.*, 12, 1443-1475, doi:10.5194/gmd-12-1443-2019

Hansen, J., Mki. Sato, R. Ruedy, L. Nazarenko, A. Lacis, G.A. Schmidt, G. Russell, I. Aleinov, M. Bauer, S. Bauer, N. Bell, B. Cairns, V. Canuto, M. Chandler, Y. Cheng, A. Del Genio, G. Faluvegi, E. Fleming, A. Friend, T. Hall, C. Jackman, M. Kelley, N.Y. Kiang, D. Koch, J. Lean, J. Lerner, K. Lo, S. Menon, R.L. Miller, P. Minnis, T. Novakov, V. Oinas, J.P. Perlwitz, Ju. Perlwitz, D. Rind, A. Romanou, D. Shindell, P. Stone, S. Sun, N. Tausnev, D. Thresher, B. Wielicki, T. Wong, M. Yao, and S. Zhang (2005), Efficacy of climate forcings, *J. Geophys. Res.*, 110, D18104, doi:10.1029/2005JD005776

Held, I. M., and B. J. Soden (2006), Robust responses of the hydrological cycle to global warming, *J. Clim.*, 19, 568–5699, doi:10.1175/JCLI3990.1

Hermans, T. H. J., J.M. Gregory, M.D. Palmer, M.A. Ringer, C.A. Katsman, and A.B.A. Slangen (2021), Projecting global mean sea-level change using CMIP6 models. *Geophys. Res. Lett.*, 48, e2020GL092064, doi:10.1029/2020GL092064

Ito, G., A. Romanou, N.Y. Kiang, G. Faluvegi, I. Aleinov, R. Ruedy, G. Russell, P. Lerner, M. Kelley, and K. Lo (2020), Global carbon cycle and climate feedbacks in the NASA GISS ModelE2.1, *J. Adv. Model. Earth Syst.*, 12, doi:10.1029/2019MS002030

Kelley, M., G.A. Schmidt, L. Nazarenko, S.E. Bauer, R. Ruedy, G.L. Russell, A.S. Ackerman, I. Aleinov, M. Bauer, R. Bleck, V. Canuto, G. Cesana, Y. Cheng, T.L. Clune, B.I. Cook, C.A. Cruz, A.D. Del Genio, G.S. Elsaesser, G. Faluvegi, N.Y. Kiang, D. Kim, A.A. Lacis, A. Leboissetier, A.N. LeGrande, K.K. Lo, J. Marshall, E.E. Matthews, S. McDermid, K. Mezuman, R.L. Miller, L.T. Murray, V. Oinas, C. Orbe, C. Pérez García-Pando, J.P. Perlwitz, M.J. Puma, D. Rind, A. Romanou, D.T. Shindell, S. Sun, N. Tausnev, K. Tsigaridis, G.

Tselioudis, E. Weng, J. Wu, and M.-S. Yao (2020), GISS-E2.1: Configurations and climatology, *J. Adv. Model. Earth Syst.*, **12**, e2019MS002025, doi:10.1029/2019MS002025

Kriegler, E., J.P. Weyant, G.J. Blanford, V. Krey, L. Clarke, J. Edmonds, A. Fawcett, G. Luderer, K. Riahi, R. Richels, S.K. Rose, M. Tavoni, and D.P. van Vuuren (2014), The role of technology for achieving climate policy objectives: Overview of the EMF27 study on global technology and climate policy strategies, *Climatic Change*, 123, 353–367

Kriegler, E., N. Bauer, A. Popp, F. Humpenöder, M. Leimbach, J. Strefler, L. Baumstark, B. Bodirsky, J. Hilaire, D. Klein, I. Mouratiadou, I. Weindl, C. Bertram, J.P. Dietrich, G. Luderer, M. Pehl, R. Pietzcker, F. Piontek, H. Lotze-Campen, A. Biewald, M. Bonsch, A. Giannousakis, U. Kreidenweis, C. Müller, S. Rolinski, A. Schultes, J. Schwanitz, M. Stefanovic, K. Calvin, E. Emmerling, S. Fujimori, and O. Edenhofer (2017**),** Fossil-fueled development (SSP5): an energy and resource intensive scenario for the 21 st century**,** *Global Environ. Change*, 42, 297-315, doi:10.1016/j.gloenvcha.2016.05.015

Large, W.G., J.C. McWilliams, and S.C. Doney (1994), Oceanic vertical mixing: a review and a model with a nonlocal boundary layer parameterization, *Rev. Geophys.,* 32, 363-403

Lenssen, N., G. Schmidt, J. Hansen, M. Menne, A. Persin, R. Ruedy, and D. Zyss (2019), Improvements in the GISTEMP uncertainty model. *J. Geophys. Res. Atmos.*, 124, 6307-6326, doi:10.1029/2018JD029522.

Lund, M.T., G. Myhre, and B. H. Samset (2019), Anthropogenic aerosol forcing under the Shared Sicioeconomic Pathways, *Atmos. Chem. Phys.*, 19, 13827–13839, doi:10.5194/acp-19-13827-2019

Manabe, S. and R.J. Stouffer (1994), Multiple-century response of a coupled ocean-atmosphere model to an increase of atmospheric carbon dioxide. J. Climate, 7, 5–23

Manabe, S. and R.J. Stouffer (1999), The role of thermohaline circulation in climate, *Tellus*, 51A-B, 91-109

Meehl, G. A., C.A. Senior, V. Eyring, G. Flato, J.-F. Lamarque, R.J. Stouffer, K.E. Taylor, and M. Schlund (2020), Context for interpreting equilibrium climate sensitivity and transient climate response from the CMIP6 earth system models, *Science Advances*, 6, 26, doi:10.1126/sciadv.aba1981

Meinshausen, M., N. Meinshuasen, W. Hare, S.C. Raper, K. Frieler, R. Knutti, D.J. Frame, and M.R. Allen (2009), Greenhouse emission targets for limiting global warming to +2°C, *Nature*, 458, 1158-1163

Meinshausen, M., S.J. Smith, K. Calvin, J.S. Daniel, M.L.T. Kainuma, J.-F. Lamarque, K. Matsumoto, S.A. Montzka, S.C.B. Raper, K. Riahi, A. Thomson, G.J.M. Velders, and D.P. van Vuuren (2011), The RCP greenhouse gas concentrations and their extensions from 1765 to 2300, *Climatic Change*, 109, 213–241

Meinshausen, M., Z. R. J. Nicholls, J. Lewis, M. J. Gidden, E. Vogel, M. Freund, U. Beyerle, C. Gessner, A. Nauels, N. Bauer, J. G. Canadell, J. S. Daniel, A. John, P. B. Krummel, G. Luderer, N. Meinshausen, S. A. Montzka, P. J. Rayner, S. Reimann, S. J. Smith, M. van den Berg, G. J. M. Velders, M. K. Vollmer, and R. H. J. Wang (2020), The shared socio-economic pathway (SSP) greenhouse gas concentrations and their extensions to 2500, *Geosci. Model Dev.*, 13, 3571–3605, doi:10.5194/gmd-13-3571-2020

Menon, S., D. Koch, G. Beig, S. Sahu, J. Fasullo, and D. Orlikowski (2010), Black carbon aerosols and the third polar ice cap, *Atmos. Chem. Phys*., 10,4559-4571, doi:10.5194/acp-10-4559-2010

Miller, R.L., G.A. Schmidt, and D.T. Shindell (2006), Forced annular variations in the 20th century Intergovernmental Panel on Climate Change Fourth Assessment Report models. *J. Geophys. Res.*, 111, D18101, doi:10.1029/2005JD006323

Miller, R.L., G.A. Schmidt, L.S. Nazarenko, N. Tausnev, S.E. Bauer, A.D. Del Genio, M. Kelley, K.K. Lo, R. Ruedy, D.T. Shindell, I. Aleinov, M. Bauer, R. Bleck, V. Canuto, Y.-H. Chen, Y. Cheng, T.L. Clune, G. Faluvegi, J.E. Hansen, R.J. Healy, N.Y. Kiang, D. Koch, A.A. Lacis, A.N. LeGrande, J. Lerner, S. Menon, V. Oinas, C. Pérez García-Pando, J.P. Perlwitz, M.J. Puma, D. Rind, A. Romanou, G.L. Russell, M. Sato, S. Sun, K. Tsigaridis, N. Unger, A. Voulgarakis, M.-S. Yao, and J. Zhang (2014), CMIP5 historical simulations (1850-2012) with GISS ModelE2. *J. Adv. Model. Earth Syst.*, **6**, no. 2, 441-477, doi:10.1002/2013MS000266

Miller, R.L., G.A. Schmidt, L. Nazarenko, S.E. Bauer, M. Kelley, R. Ruedy, G.L. Russell, A. Ackerman, I. Aleinov, M. Bauer, R. Bleck, V. Canuto, G. Cesana, Y. Cheng, T.L. Clune, B. Cook, C.A. Cruz, A.D. Del Genio, G.S. Elsaesser, G. Faluvegi, N.Y. Kiang, D. Kim, A.A. Lacis, A. Leboissetier, A.N. LeGrande, K.K. Lo, J. Marshall, E.E. Matthews, S. McDermid, K. Mezuman, L.T. Murray, V. Oinas, C. Orbe, C. Pérez García-Pando, J.P. Perlwitz, M.J. Puma, D. Rind, A. Romanou, D.T. Shindell, S. Sun, N. Tausnev, K. Tsigaridis, G. Tselioudis, E. Weng, J. Wu, and M.-S. Yao (2021), CMIP6 historical simulations (1850–2014) with GISS-E2.1. *J. Adv. Model. Earth Syst.*, **13**, e2019MS002034. doi:10.1029/2019MS002034

Nakicenovic et al (2000), Special Report on Emissions Scenarios (SRES). Cambridge University Press, Cambridge

Nazarenko, L., G.A. Schmidt, R.L. Miller, N. Tausnev, M. Kelley, R. Ruedy, G.L. Russell, I. Aleinov, M. Bauer, S. Bauer, R. Bleck, V. Canuto, Y. Cheng, T.L. Clune, A.D. Del Genio, G. Faluvegi, J.E. Hansen, R.J. Healy, N.Y. Kiang, D. Koch, A.A. Lacis, A.N. LeGrande, J. Lerner, K.K. Lo, S. Menon, V. Oinas, J.P. Perlwitz, M.J. Puma, D. Rind, A. Romanou, M. Sato, D.T. Shindell, S. Sun, K. Tsigaridis, N. Unger, A. Voulgarakis, M.-S. Yao, and J. Zhang (2015), Future climate change under RCP emission scenarios with GISS ModelE2, *J. Adv. Model. Earth Syst.*, **7**, 244-267, doi:10.1002/2014MS000403

Nicholls, Z. R. J., M. Meinshausen, J. Lewis, R. Gieseke, D. Dommenget, K. Dorheim, C.-S. Fan, J.S. Fuglestvedt, T. Gasser, U. Golüke, P. Goodwin, C. Hartin, A.P. Hope, E. Kriegler, N.J. Leach, D. Marchegiani, L.A. McBride, Y. Quilcaille, J. Rogelj, R.J. Salawitch, B.H. Samset, M. Sandstad, A.N. Shiklomanov, R.B. Skeie, C.J. Smith, S. Smith, K. Tanaka, J. Tsutsui, and Z. Xie (2020), Reduced Complexity Model Intercomparison Project Phase 1: introduction and evaluation of global-mean temperature response, *Geosci. Model Dev.*, 13, 5175–5190, doi:10.5194/gmd-13-5175-2020

Notz, D., and SIMIP Community (2020), Arctic sea ice in CMIP6, *Geophys. Res. Let.*, 47, e2019GL086749, doi:10.1029/2019GL086749

O'Neill, B.C., C. Tebaldi, D. van Vuuren, V. Eyring, P. Friedlingstein, G. Hurtt, R. Knutti, E. Kriegler, J.-F. Lamarque, J. Lowe, J. Meehl, R. Moss, K. Riahi, and B.M. Sanderson (2016), The scenario model intercomparison project (ScenarioMIP) for CMIP6, *Geosci. Model Dev.*, 9, 3461-3482, doi:10.5194/gmd-9-3461-2016

O'Neill, B.C., T.R. Carter, K. Ebi , P.A. Harrison, E. Kemp-Benedict, K. Kok, E. Kriegler, B.L. Preston, K. Riahi, J. Sillmann, B.J. van Ruijven, D. van Vuuren, D. Carlisle, C. Conde, J.

Fuglestvedt, C. Green, T. Hasegawa, J. Leininger15, S. Monteith, and R. Pichs-Madruga (2020), Achievements and needs for the climate change scenario framework. *Nat. Clim. Chang.* **10,** 1074–1084, doi:10.1038/s41558-020-00952-0

Paris Agreement to the United Nations Framework Convention on Climate Change, Dec. 12, 2015, T.I.A.S. No. 16-1104

Partanen, A.I., J.-S. Landry, and H.D. Matthews (2018), Climate and health implications of future aerosol emission scenarios, *Environ. Res. Lett.*, 13, 024028, doi:10.1088/1748-9326/aaa511

Popp, A., K. Calvin, S. Fujimori, P. Havlik, F. Humpenöder, E. Stehfest, B.L. Bodirsky, J.F. Dietrich, J.C. Doelmann, M. Gusti, T. Hasegawa, P. Kyle, M. Obersteiner, A. Tabeau, K. Takahashi, H. Valin, S. Waldhoff, I. Weindl, M. Wise, E. Kriegler, H. Lotze-Campen, O. Fricko, K. Riahi, and D.P. van Vuuren (2017), Land-use futures in the shared sicio-economic pathways, *Global Environ. Change*, 42, 331-345, doi:10.1016/j.gloenvcha.2016.10.002

Riahi, K., D.P. van Vuuren, E. Kriegler, J. Edmonds, B. O'Neill, S. Fujimori, N. Bauer, K. Calvin, R. Dellink, O. Fricko, W. Lutz, A. Popp, J. Crespo Cuaresma, M. Leimbach, T. Kram, S. Rao, J. Emmerling, T. Hasegawa, P. Havlik, F. Humpenöder, L. Aleluia Da Silva, S.J. Smith, E. Stehfest, V. Bosetti, J. Eom, D. Gernaat, T. Masui, J. Rogelj, J. Strefler, L. Drouet, V. Krey, G. Luderer, M. Harmsen, K. Takahashi, M. Wise, L. Baumstark, J. Doelman, M. Kainuma, Z. Klimont, G. Marangoni, R. Moss, H. Lotze-Campen, M. Obersteiner, A. Tabeau, and M. Tavoni (2017), The Shared Socio-Economic Pathways and their energy, land use and greenhouse gas emissions implications: an overview, *Global Environ. Change*, 42, 153-168, doi:10.1016/j.gloenvcha.2016.05.009

Russell, G.L., J.R. Miller, and D.H. Rind (1995), A coupled atmosphere-ocean model for transient climate change, *Atmosphere-ocean*, 33, 683-730

Rye, C.D., J. Marshall, M. Kelley, G. Russell, L.S. Nazarenko, Y. Kostov, G.A. Schmidt, and J. Hansen (2020), Antarctic glacial melt as a driver of recent Southern Ocean climate trends, *Geophys. Res. Let.*, 47, e2019GL086892, doi:10.1029/2019GL086892

Schmidt, G. A., C.M. Bitz, U. Mikolajewicz, and L.B. Tremblay (2004), Ice-ocean boundary conditions for coupled models. *Ocean Modelling*, *7*, 59–74

Schmidt, G.A., M. Kelley, L. Nazarenko, R. Ruedy, G.L. Russell, I. Aleinov, M. Bauer, S.E. Bauer, M.K. Bhat, R. Bleck, V. Canuto, Y.-H. Chen, Y. Cheng, T.L. Clune, A. Del Genio, R. de Fainchtein, G. Faluvegi, J.E. Hansen, R.J. Healy, N.Y. Kiang, D. Koch, A.A. Lacis, A.N. LeGrande, J. Lerner, K.K. Lo, E.E. Matthews, S. Menon, R.L. Miller, V. Oinas, A.O. Oloso, J.P. Perlwitz, M.J. Puma, W.M. Putman, D. Rind, A. Romanou, M. Sato, D.T. Shindell, S. Sun, R.A. Syed, N. Tausnev, K. Tsigaridis, N. Unger, A. Voulgarakis, M.-S. Yao, and J. Zhang (2014), Configuration and assessment of the GISS ModelE2 contributions to the CMIP5 archive, *J. Adv. Model. Earth Syst.*, 6, 141-184, doi:10.1002/2013MS000265

Séférian, R., P. Nabat, M. Michou, D. Saint-Martin, A. Voldoire, J. Colin, B. Decharme, C. Delire, S. Berthet, M. Chevallier, S. Sénési, L. Franchisteguy, J. Vial, M. Mallet, E. Joetzjer, O. Geoffroy, J.-F. Guérémy, M.-P. Moine, R. Msadek, A. Ribes, M. Rocher, R. Roehrig, D. Salas-y-Mélia, E. Sanchez, L. Terray, S. Valcke, R. Waldman, O. Aumont, L. Bopp, J. Deshayes, C. Éthé, and G. Madec (2020), Evaluation of CNRM Earth-System model, CNRM-ESM2-1: role of Earth system processes in present-day and future climate, *J. Adv. Model. Earth Syst.*, 11, 4182–4227, doi:10.1029/2019MS001791

Sherwood, S., M.J. Webb, J.D. Annan, K.C. Armour, P.M. Forster, J. Hargreaves, G. Hegerl, S. A. Klein, K. D. Marvel, E. J. Rohling, M. Watanabe, T. Andrews, P. Braconnot, C. S. Bretherton, G. L. Foster, Z. Hausfather, A. S. von der Heydt, R. Knutti, T. Mauritsen, J. R. Norris, C. Proistosescu, M. Rugenstein, G. A. Schmidt, K. B. Tokarska, and M. D. Zelinka (2020). A combined assessment of Earth's climate sensitivity, *Reviews of Geophysics*. https://doi.org/10.1029/2019RG000678

Shindell, D. T., O. Pechony, A. Voulgarakis, G. Faluvegi, L. Nazarenko, J.-F. Lamarque, K. Bowman, G. Milly, W. Kovari, R. Ruedy, and G. A. Schmidt (2013), Interactive ozone and methane chemistry in GISS-E2 historical and future climate simulations, *Atmos. Chem. Phys*., 13, 2653-2689, doi:10.5194/acp-13-2653-2013

Shindell, D. T., and G. A. Schmidt (2004), Southern Hemisphere climate response to ozone changes and greenhouse gas increases, *Geophys. Res. Lett.*, 31, L18209, doi:10.1029/2004GL020724

Smith, C.J., R.J. Kramer, G. Myhre, P.M. Forster, B.J. Soden, T. Andrews, O. Boucher, G. Faluvegi, D. Fläschner, Ø. Hodnebrog, M. Kasoar, V. Kharin, A. Kirkevåg, J.-F. Lamarque, J. Mülmenstädt, D. Olivié, T. Richardson, B.H. Samset, D. Shindell, P. Stier, T. Takemura, A. Voulgarakis, and D. Watson-Parris (2018), Understanding Rapid Adjustments to Diverse Forcing Agents, *Geophys. Res. Let.*, 45, 12,023-012,031, 10.1029/2018gl079826

Stevens, B., et al. (2013), Atmospheric componenet of the MPI-M Earth system model: ECHAM6, *J. Adv. Model. Earth Syst.*, *5*, 146-172, doi:10.1002/jame.20015

Stroeve, J., and D. Notz (2015), Insights on past and future sea-ice evolution from combining observations and models, *Global and Planetary Change*, 135, 119–132, doi:10.1016/j.gloplacha.2015.10.011

Sun, S., and R. Bleck (2006), Multi-century simulations with the coupled GISS-HYCOM climate model: Control experiments, *Clim. Dynam.*, 26, 407-428, doi:10.1007/s00382-005-0091-7

Tebaldi, C., K. Debeire, V. Eyring, E. Fischer, J. Fyfe, P. Friedlingstein, R. Knutti, J. Lowe, B. O'Neill, B. Sanderson, D. van Vuuren, K. Riahi, M. Meinshausen, Z. Nicholls, K. B. Tokarska, G. Hurtt, E. Kriegler, J.-F. Lamarque, G. Meehl, R. Moss, S. E. Bauer, O. Boucher, V. Brovkin, Y.-H. Byun, M. Dix, S. Gualdi, H. Guo, J. G. John, S. Kharin, Y. Kim, T. Koshiro, L. Ma, D. Olivié, S. Panickal, F. Qiao, X. Rong, N. Rosenbloom, M. Schupfner, R. Séférian, A. Sellar, T. Semmler, X. Shi, Z. Song, C. Steger, R. Stouffer, N. Swart, K. Tachiiri, Q. Tang, H. Tatebe, A. Voldoire, E. Volodin, K. Wyser, X. Xin, S. Yang, Y. Yu, and T. Ziehn (2021), Climate model projections from the Scenario Model Intercomparison Project (ScenarioMIP) of CMIP6, *Earth Syst. Dynam.*, 12, 295-312, doi:10.5194/esd-12-295-2021

Tokarska, K.B., M. B. Stolpe, S. Sippel, E. M. Fischer, C. J. Smith, F. Lehner, R. Knutti (2020), Past warming trend constrains future warming in CMIP6 models, *Science Advances*, 6, doi:10.1126/sciadv.aaz9549

Thompson, D. W. J., and J. M. Wallace (2000), Annular modes in the extratropical circulation. Part I: Month-to-month variability, *J. Clim.*, 13, 1000–1016.

Twomey, S. (1977), The Influence of Pollution on the Shortwave Albedo of Clouds, *J. Atmos. Sci*., 34 (7): 1149–52

van Vuuren, D.P., J. Edmonds, M. Kainuma, K. Riahi, A. Thomson, K. Hibbard, G.C. Hurtt, T. Kram, V. Krey, J.-F. Lamarque, T. Masui, M. Meinshausen, N. Nakicenovic, S.J. Smith, and S.K. Rose (2011a), The representative concentration pathways: an overview, *Clim. Change*, 109: 5-31, doi 10.1007/s10584-011-0148-z

van Vuuren, D.P., E. Stehfest, D. Gernaat, J. Doelman, M. van Den Berg, M. Harmsen, H.S. de Boer, A.F. Bouwman, V. Daioglou, O.Y. Edelenbosch, B. Girod, T. Kram, L. Lassaletta, P. Lucas, H. van Meijl, C. Müller, B. van Ruijven, S. van der Sluis, and A. Tabeau (2017), Energy, land-use and greenhouse gas emissions trajectories under a green growth paradigm, *Global Environ. Change*, 42, 237-250, doi:10.1016/j.gloenvcha.2016.05.008

Weijer, W., W. Cheng, O.A. Garuba, A. Hu, and B.T. Nadiga (2020), CMIP6 models predict significant 21st century decline of the Atlantic Meridional Overturning Circulation, *Geophys. Res. Let.*, 47, e2019GL086075, doi:10.1029/2019GL086075

Zanna, L., S. Khatiwala, J.M. Gregory, J. Ison, and P. Heimbach (2019), Global reconstruction of historical ocean heat storage and transport, *Proceedings of the National Academy of Sciences of the United States of America*, 116(4), 1126–1131, doi:10.1073/pnas.1808838115

Zelinka, M.D., T.A. Myers, D.T. McCoy, S. Po-Chedley, P.M. Caldwell, P. Ceppi, S.A. Klein, and K.E. Taylor (2020), Causes of higher climate sensitivity in CMIP6 models, *Geophys. Res. Let.*, 47, e 2019GL085782, https://doi.org/10.1029/2019GL085782.

Zhang, J., and D. Rothrock (2000), Modeling Arctic sea ice with an efficient plastic solution, *J. Geophys. Res.*, 105: 3325–3338